



**THE FOCUSING OF LIGHT SCATTERED FROM DIFFUSE
REFLECTORS USING PHASE MODULATION**

THESIS

Jessica Schafer, Second Lieutenant, USAF
AFIT/APPLPHY/ENP/12-M10

**DEPARTMENT OF THE AIR FORCE
AIR UNIVERSITY**

AIR FORCE INSTITUTE OF TECHNOLOGY

Wright-Patterson Air Force Base, Ohio

DISTRIBUTION STATEMENT A.
APPROVED FOR PUBLIC RELEASE; DISTRIBUTION UNLIMITED.

The views expressed in this thesis are those of the author and do not reflect the official policy or position of the United States Air Force, Department of Defense, or the United States Government. This material is declared a work of the U.S. Government and is not subject to copyright protection in the United States.

AFIT/APPLPHY/ENP/12-M10

THE FOCUSING OF LIGHT SCATTERED FROM DIFFUSE REFLECTORS
USING PHASE MODULATION

THESIS

Presented to the Faculty
Department of Engineering Physics
Graduate School of Engineering and Management
Air Force Institute of Technology
Air University
Air Education and Training Command
in Partial Fulfillment of the Requirements for the
Degree of Master of Science in Applied Physics

Jessica Schafer, BSP
Second Lieutenant, USAF

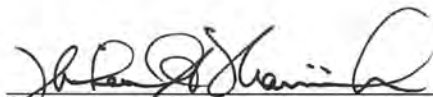
March 2012

DISTRIBUTION STATEMENT A.
APPROVED FOR PUBLIC RELEASE; DISTRIBUTION UNLIMITED.

THE FOCUSING OF LIGHT SCATTERED FROM DIFFUSE REFLECTORS
USING PHASE MODULATION

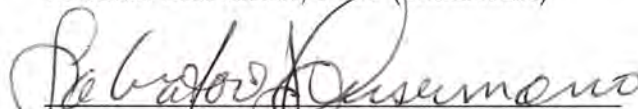
Jessica Schafer, BSP
Second Lieutenant, USAF

Approved:




Michael Marciniak, PhD (Chairman)

7 Mar 12
Date



Salvatore Cusumano, PhD (Member)

7 Mar 12
Date



Maj Milo Hyde, PhD (Member)

12 Mar 12
Date

Abstract

An imaging technique called indirect photography was recently demonstrated for imaging otherwise hidden scene information through the collection and radiometric modeling of light reflecting off of visible reflecting surfaces. A laser is reflected from a visible surface onto the hidden object. A camera then collects light which reflects from the object back to the visible surface. The camera images are used to construct an indirect image of the hidden object. The ability to focus the beam that reflects off the visible surface to a tight spot on the hidden object is theorized to simulate a direct line of sight from the light source to the object, effectively reducing the radiometric model to that of the previously demonstrated dual photography, and leading to much-simplified results. This work demonstrates that capability.

Experiments involving the focusing of light transmitted through highly scattering media have been adapted to the case of reflection. The focusing of a HeNe laser reflected off diffusely scattering surfaces to a tight spot is demonstrated using phase control. A liquid crystal spatial light modulator assigns phase delay pixel by pixel to the Gaussian beam to conjugate the scattering properties of the reflector. Intensity enhancement values between 13.8 and 122.3 are achieved for the surfaces studied. While samples with relatively strong specular reflection achieve higher enhancement for a given geometry, the more diffusely reflecting materials achieve higher enhancement in regions of nonspecular scatter. High diffuse scatter thus facilitates the non-mechanical steering of the focused spot.

Acknowledgements

First and foremost, I would like to express my sincerest gratitude for the guidance and encouragement afforded to me by my faculty advisor, Dr. Michael Marciniak. Thanks must go to Mr. Greg Smith and Mr. Mike Ranft for their deft hands, refreshing demeanors, and resourceful insights. Without their help, my lab setup may have been held together with duct tape. I would also like to thank Paul Thelen for bringing me Subway and Taco Bell during long, unexpected nights in the laboratory and the Sorensens for amazing home-cooked meals when I could break away. Paul and I had some unforgettable power coding parties—we'd occasionally take much-needed breaks to practice our shuffling skills or watch baby animal videos. Mark Spencer and Mike Steinbock provided highly appreciated insights and suggestions throughout the course of my research. I'd also like to enthusiastically thank Dr. Vellekoop for answering questions about his work upon which the experiments in this thesis are based. Finally, to my boyfriend: thank you for being incredible. Seriously...incredible.

Jessica Schafer

Table of Contents

	Page
Abstract	iv
Acknowledgements	v
List of Figures	viii
I. Introduction	1
1.1 Research Motivation	1
1.2 Problem Statement	2
1.3 Methodology	3
1.4 Overview	3
II. Literature Review	4
2.1 Introduction	4
2.2 Dual Photography	4
2.3 Indirect Photography	6
2.4 Inverse Diffusion using an SLM	7
2.5 Liquid Crystal Spatial Light Modulator	10
2.6 Nonmechanical Beam Steering	10
2.7 Reflective Inverse Diffusion within Indirect Photography	13
2.8 Diffusely Reflecting Materials	13
2.9 Summary	15
III. Methodology	16
3.1 Introduction	16
3.2 Laboratory Equipment	16
3.3 SLM Characterization	16
3.4 Optical Setup	19
3.5 Automated Experimental Control	21
3.6 Phase Manipulation Algorithms	22
3.7 System Limitations	24
3.8 Reflection Materials	25
3.9 Nonmechanical Beam Steering	26
3.10 Speckle Pattern Decorrelation Test	28
3.11 Summary	29

	Page
IV. Results and Analysis	30
4.1 Introduction	30
4.2 Optimization Considerations	30
4.3 Speckle Size	33
4.4 Comparison of Reflective Surfaces	33
4.5 Spot Size Analysis	36
4.6 Nonmechanical Beam Steering	39
4.7 Speckle Pattern Decorrelation	43
4.8 Summary	44
V. Discussion	46
5.1 Introduction	46
5.2 Results Summary	46
5.3 Conclusions Drawn from Results	46
5.4 Recommendations for Future Work	47
5.4.1 Algorithm Improvement	47
5.4.2 Technique Improvement	48
5.4.3 Reflective Inverse Diffusion Characterization	50
5.4.4 Implementation in Indirect Photography	50
5.5 Final Comments	51
A. Reflective Inverse Diffusion MATLAB Function	52
B. Reflective Inverse Diffusion MATLAB Subfunctions	56
C. Surface Profiles of Reflectors	61
D. Relative Intensity Plots and Images	62
Bibliography	66

List of Figures

Figure		Page
1.	Principle of Dual Photography.	5
2.	Dual vs. Indirect Setup.	6
3.	Indirect photography setup.	7
4.	Opaque lensing.	8
5.	SLM schematic.	11
6.	Beam steering schematic.	11
7.	Bidirectional reflectance distribution function.	12
8.	SLM feedback progression.	14
9.	Twyman-Green interferometer.	17
10.	Calibration fringe patterns.	18
11.	Phase response data.	19
12.	Transmissve inverse diffusion setup.	20
13.	Reflective inverse diffusion setup.	21
14.	Pixel scheme.	22
15.	Target intensity weighting.	23
16.	Grouped pixel dimensions.	24
17.	Algorithm schematic for one grouped SLM pixel.	25
18.	Reflective Surfaces.	26
19.	Beam steering across playing card.	27
20.	Speckle decorrelation test.	28
21.	Pre-optimizing the SLM.	31
22.	Target intensity variation with phase delay.	32

Figure		Page
23.	Speckle size varies with N	33
24.	Sample enhancement comparison.	35
25.	Sample relative intensity comparison.	37
26.	Spot size relationships.	38
27.	Signal autocorrelation.	39
28.	Beam steering to CCD corners.	40
29.	Beam steering along dimensions of a playing card.	42
30.	Enhancement comparison of specular to diffuse reflection.	43
31.	Speckle decorrelation.	44
32.	Adaptive algorithm.	48
33.	Surface profiles.	61
34.	Relative intensity data for brushed aluminum.	62
35.	Relative intensity data for sandblasted aluminum.	63
36.	Relative intensity data for infragold.	63
37.	Relative intensity data for white paint on reflection.	64
38.	Relative intensity data for graphite.	64
39.	Relative intensity data for spectralon.	65

THE FOCUSING OF LIGHT SCATTERED FROM DIFFUSE REFLECTORS USING PHASE MODULATION

I. Introduction

1.1 Research Motivation

The aim of this thesis is to focus light scattered off of diffuse surfaces by adjusting the phase elements of the beam with a liquid crystal (LC) spatial light modulator (SLM). This focusing capability is theorized to have implications for advancing efforts in an imaging technique called “indirect photography.” The concept of indirect photography has recently been introduced as a photographic technique for imaging objects hidden around corners. Indirect photography stems from a technique called “dual photography,” a method which exploits Helmholtz reciprocity by using a light source to illuminate a scene and measuring the light transport between each pair of source-to-camera pixels. The “dual image” is generated with the computational interchanging of the source and camera. Attaining an “indirect image” involves collocating the camera and the light source to recover parts of the scene not directly visible to either the camera or the controlling light source [1].

Collocating the light source and the camera gives rise to a potentially powerful imaging technique which could become a valuable asset in U.S. military operations. In effect, a soldier could “see around corners” by imaging an object with light reflected off of a diffuse surface. This technique uses the radiometric principles developed in dual photography while adding another diffuse surface reflection to factor into the imaging process [2]. The ability to focus the light source onto the object after reflection off of

the first diffuse surface is assumed to be equivalent to using a light source with a direct line of sight to the object, thereby reducing the problem of indirect photography to dual photography.

Recent experiments by Vellekoop *et al.* have shown that on transmission, solving for and applying a uniquely shaped wavefront can be used to steer light through a highly scattering object in a process called “inverse diffusion.” The wavefront is shaped to exactly match the scattering properties of the object so that the object focuses the light to a point [3]. Inspired by this research, the method introduced here to focus light scattered upon diffuse reflection parallels the technique developed for inverse diffusion in transmission. For the purpose of this thesis, we will refer to inverse diffusion as demonstrated by Vellekoop as “transmissive inverse diffusion” while using the term “reflective inverse diffusion” to signify the adaptation of the technique to the case of reflection.

1.2 Problem Statement

This thesis seeks to accomplish a set of four overarching goals including (1) the demonstration of a proof of concept for focusing light scattered off of an assortment of diffusely reflecting surfaces with various scattering properties, (2) the nonmechanical steering of the focused spot, (3) the identification of certain material and experimental factors which must be considered when applying reflective inverse diffusion to indirect photography, and (4) a prescriptive outline sketching out the progression required to use the results from this thesis and extend them to practical implementation in indirect photography.

1.3 Methodology

The optical setup used for demonstrating reflective inverse diffusion is designed to contain aspects of Vellekoop’s experiment for transmissive inverse diffusion while removing constraints which would render it unuseful for indirect photography. Optical components such as a microscope objective placed shortly before and shortly after the scattering sample are removed. The technique is demonstrated on six nonspecular reflective surfaces and the differences in the performance of the technique are analyzed with respect to material properties. The main idea of the experiment is to achieve focused spots from diffuse reflection off of various reflecting materials while using a feasible indirect photography setup, and to steer the focused spot to different locations on a simulated object by choosing different target areas for the same setup.

1.4 Overview

This thesis is broken up into five chapters. The second chapter discusses background from literature on dual photography, indirect photography, radiometry, and the properties of the surfaces used in this experiment. Chapter 3 describes the testing methodology. Chapter 4 details the results of the experiments, and Chapter 5 offers recommendations for improving the technique used in this thesis and for further developing it.

II. Literature Review

2.1 Introduction

This chapter reviews previous research which shapes and applies to the technique developed in this thesis for focusing light scattered from a diffuse surface. While this technique does not require detailed knowledge of the theoretical underpinnings of dual and indirect photography, a brief review of the theory and literature are offered to contextualize the problem and experimental setup. The principles of transmissive inverse diffusion on which the reflective inverse diffusion technique is based are discussed. Nonmechanical beam steering using a LC SLM is also introduced and related to beam steering via reflection off of highly scattering surfaces. Finally, characteristics of the diffuse surfaces chosen to demonstrate reflective inverse diffusion are highlighted.

2.2 Dual Photography

Dual photography as developed by Sen *et al.* is a completely image-based mathematical method for generating pictures from the viewpoint of a light-emitting projector rather than a camera. A pixelated light source is used to illuminate a scene while a digital camera is used to record images from reflection of the scene or from reflection off of a diffuse surface. The images are used to construct a transport matrix T which maps light source pixel to camera pixel transport characteristics. As illustrated on the left in Figure 1, the linearity of light transport allows for a matrix mapping between source and camera given by

$$c' = Tp' \tag{1}$$

in which p' is an $m \times 1$ vector representing the light source with $m \times n$ pixels, c' is a $p \times q$ vector representing a camera with $p \times q$ pixels, and T is the transport matrix of size $p \times q \times m \times n$ which tracks each possible transport path from source pixel to camera pixel [2].

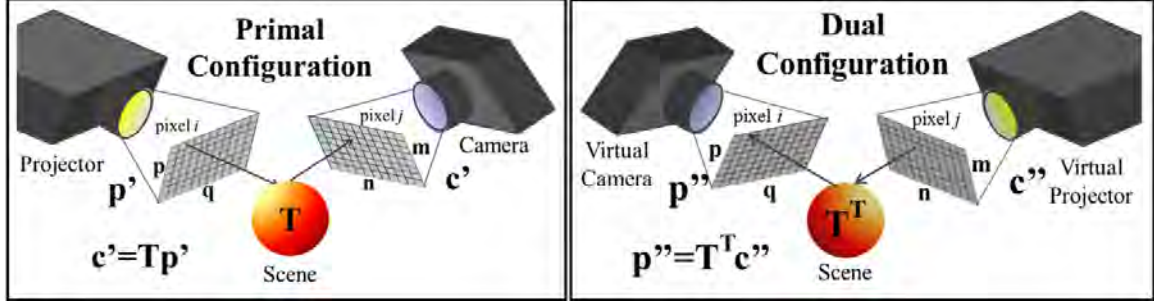


Figure 1. In the primal configuration, light is emitted by a real projector and captured with a real camera. The matrix T describes the light transport from projector to camera, where T_{ij} is the transport coefficient from projector pixel j to camera pixel i . In the dual configuration, the camera and projector are reversed, and Helmholtz reciprocity specifies that $T''_{ji} = T_{ij}$, meaning $T'' = T^T$.

As the right side of Figure 1 indicates, switching the positions of the source and camera is achieved mathematically by recognizing the light transport characteristics between each set of pixels remain unchanged, and the transpose of the transport matrix can be used to solve for an image of the scene from the perspective of the projector in accordance with

$$p'' = T^T c''. \quad (2)$$

The user can manipulate images of the scene with a variety of simulated light source characteristics making this a particularly useful technique in attaining photorealism in computer graphics applications. Sen *et al.* performed an experiment using dual photography to image the illuminated face of a playing card upon its reflection off the page of a book. While the camera did not have access to the face of the card, the card was set so that the only light that reached the camera had undergone diffuse bounces

at the card and at the book. The transport matrix was acquired from 5742 images to produce a dual image with resolution 66x87 from the perspective of the projector [4]. Taking away the constraint that the projector or light source requires a direct line of sight to the object being imaged—the playing card, in this case—would give rise to an imaging technique which would serve as a powerful capability in military operations. Figure 2 shows the relationship between a dual setup and an indirect setup.

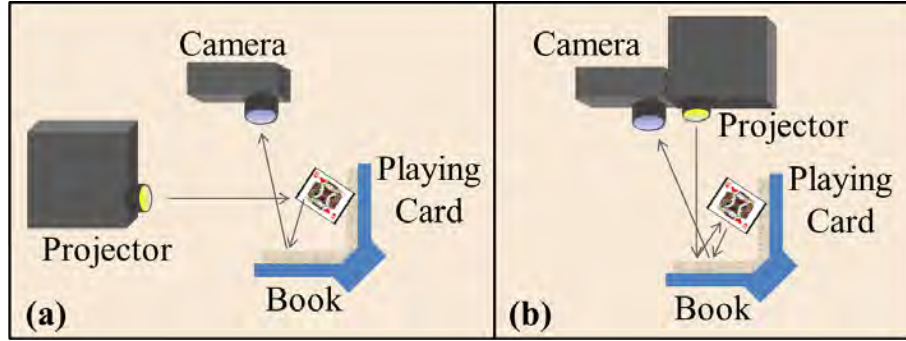


Figure 2. Real world application of (a) dual photography and (b) indirect photography.

2.3 Indirect Photography

Indirect photography is an extension of dual photography which removes the requirement that the light source has a direct line of sight to the object being imaged. The technique involves collocating the camera and a HeNe light source. The most recent set of experiments used the setup shown in Figure 3, for which the camera and laser are placed without a direct line of sight to the checkerboard underneath the top surface. The laser hits a spot on the first surface (x_1, y_1) and is reflected onto the top surface (x_2, y_2, z_2) where the checkerboard sits. Light which is reflected off the top surface and onto the first surface within the camera's field of view (x_3, y_3) is collected by the camera.

For both dual and indirect photography, the final reflecting surface is imaged. The

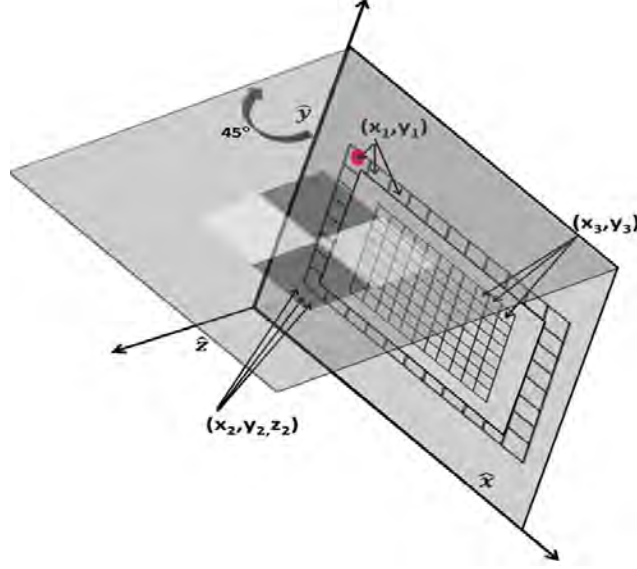


Figure 3. Most recent experimental setup for indirect photography. The laser reflects off the first surface at the points labeled (x_1, y_1) , the object to be imaged which is here a 2x2 checkerboard with coordinates labeled (x_2, y_2, z_2) , and finally back to the first surface at the points labeled (x_3, y_3) . The first and last surface are coplanar with the latter being defined by the camera field of view.

application of radiometric theory and a blind deconvolution process to these images yields an image of the object. For a thorough detailing of the radiometric development involved in attaining dual and indirect images, see [2].

2.4 Inverse Diffusion using an SLM

The ultimate goal of this thesis is to provide a framework for simplifying and improving the indirect photography technique through focusing light to a point after reflection off a diffuse surface. The ability to focus to a point on reflection effectively reduces the problem of indirect photography to that of dual photography by removing the complexity which comes with reflecting the light source off the first diffuse surface. We assume that focusing upon reflection off of a diffuse surface to a point on the object is equivalent to illuminating the object with a source with a direct line of sight. We conjecture that focusing upon reflection can be done in a manner similar

to the focusing of light in transmission by way of inverse diffusion using an SLM and that many of the same governing relationships apply.

Transmissive inverse diffusion is a technique by which an LC SLM is used to shape a wavefront to focus light through opaque objects. When an unshaped beam is transmitted through a disordered scattering medium, the result is a complicated, random interference pattern of many waves forming laser speckle. Using the LC SLM, the beam is broken into hundreds or thousands of light beams with phase delays with respect to the each other. The resulting total field at a point behind the sample is the sum of the speckle patterns of these individual beams [3]. Figure 4 illustrates how shaping the beam which impinges on the scattering sample serves to alter the "random walk" of the light through the sample. The end result is the constructive interference of transmitted light at the designated focal point.

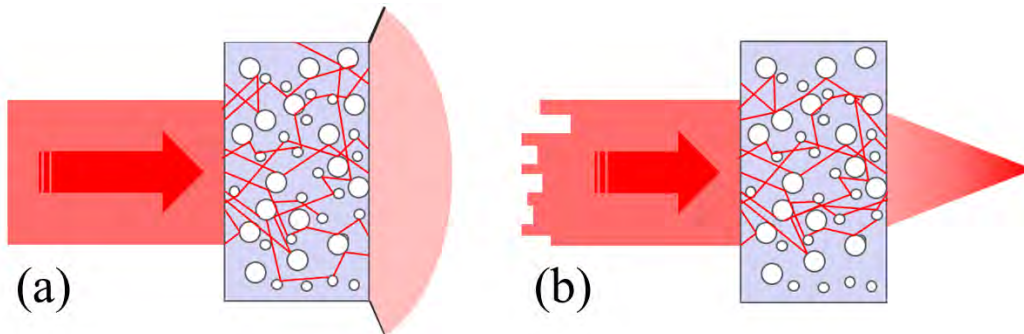


Figure 4. Opaque lensing. a) A plane wave impinging on a scattering object performs a random walk through the material. The light that makes it through is scattered in all directions. b) The wave is shaped to match the scattering in the material so that the object focuses the wave to any designated point.

Assigning phase delay to induce speckle patterns which align to one focused spot, the total field E_m in the target area is given by

$$E_m = \sum_{n=1}^{N_T} t_{mn} A_n e^{i\phi_n} \quad (3)$$

where N_T represents the total number of modulated segments of the SLM, t_{mn} is the transmission coefficient, and A_n and ϕ_n are the amplitude and phase of the laser light reflected from the SLM segment n . The constants t_{mn} are statistically independent and follow a circular Gaussian distribution, leading to an expression for the average amplitude enhancement $\langle\alpha\rangle$ given by

$$\langle\alpha\rangle = \frac{\langle|E_{opt}|\rangle_{rms}}{\langle|E_{rnd}|\rangle_{rms}} = \sqrt{\frac{\pi}{4}(N_T - 1) + 1} \approx \sqrt{\frac{\pi}{4}N_T}. \quad (4)$$

where $\langle|E_{opt}|\rangle_{rms}$ is the RMS value for the field amplitude within the optimized target area and $\langle|E_{rnd}|\rangle_{rms}$ is the RMS field amplitude of the random speckle pattern before optimization begins. The maximum intensity enhancement $\eta = \alpha^2$ is the ratio between the optimized intensity and the average intensity of the speckle pattern before optimization [5].

Comparing the final optimized intensity to the surrounding speckle intensity is of greater consequence when considering its role in indirect photography. The goal is to focus to a point on the object and minimize contributions from light reflecting off of the object outside the focus. The reflective inverse diffusion enhancement η_R is thus defined as the ratio between the optimized intensity and the average intensity of the speckle pattern surrounding the focus.

To account for the time-dependent decorrelation of the speckle pattern due to environmentally-induced instability, Vellekoop estimates that the effective enhancement decreases according to

$$\eta_{eff} = \frac{\eta}{1 + \frac{N_T T}{T_s}} \quad (5)$$

where T is the time required for a single measurement and T_s is the time scale for which the speckle pattern of the sample remains stable. The persistence time is

defined as the decay time of the transmitted speckle autocorrelate and depends on both the type of sample used and on the environmental conditions. The persistence time of the paint sample Vellekoop presents is reported to be 90 minutes due primarily to humidity in the sample [6]. The persistence time of the speckle patterns from reflection off of diffuse surfaces is expected to be higher than for transmission through highly scattering materials. In the latter, the beam undergoes hundreds of scattering events within the sample, requiring that the sample is stable with sub-wavelength accuracy throughout the optimization process [3].

2.5 Liquid Crystal Spatial Light Modulator

The LC SLM is becoming a highly researched and tested optical component for military imaging sensors as a result of its small size, light weight, and adaptability [7], making it a good candidate for its potential role in indirect photography. The LC devices used in these experiments are of the Nematic variety, which are uniaxially birefringent. Applying an external AC electric field induces a dipole in the LC molecule to produce a torque and resulting rotation of the optical axis. The incident wavefront experiences an optical path difference (OPD) based on the orientation of the LC molecule. The OPD can be adjusted on a pixel-by-pixel basis, typically achieving up to a 2π phase depth. Wavefront control is thus accomplished modulo- 2π [8]. Figure 5 shows a top-view schematic of a reflective LC SLM.

2.6 Nonmechanical Beam Steering

To further aid in simplifying indirect photography, the ability to nonmechanically steer the focused spot would allow for scanning the hidden object to be imaged without adjusting the position of any optical elements. When working with a coherent beam without an intermediate diffuse reflection, applying a saw-tooth phase profile

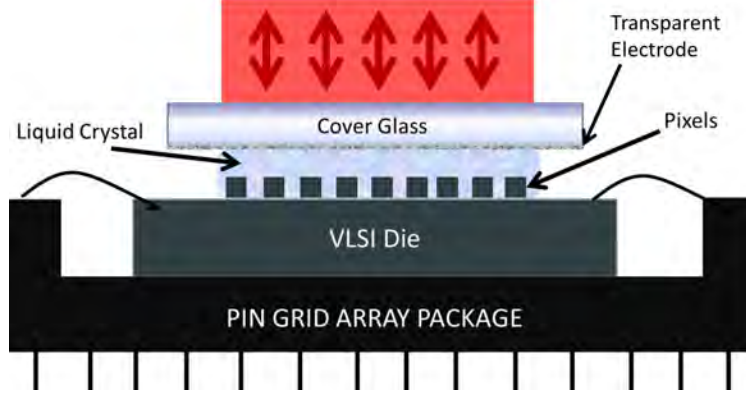


Figure 5. Top view schematic of SLM. Light is reflected by the electrode mirrors of the pixels and experiences phase delay in the liquid crystal. The VLSI die and pin grid array package control the voltage differences which align the liquid crystal molecules according to the desired index of refraction and resulting phase delay at each pixel.

to the SLM effectively induces an effect similar to a blazed diffraction grating. The wavefront is tilted and deflected to a nonzero angle as illustrated in Figure 6. A more significant steer angle is achieved with narrower phase ramps ranging from 0 to 2π phase delay. Since the SLM has a finite number of addressable pixels and the smooth ramp becomes more noticeably discretized with fewer intermediate phase delay values, the steer angle is limited.

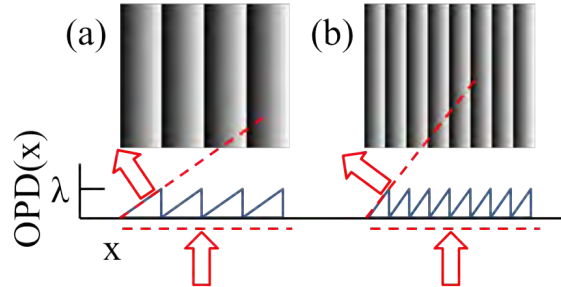


Figure 6. Beam steering schematic. The tilted wavefront (dashed red) results from application of a modulo 2π saw-tooth phase pattern. A greater tilt is induced with narrower modulated columns, which is limited by the number of addressable pixels of the SLM.

The steer angle θ of a beam using this technique is geometrically described with $\theta = \arcsin \frac{\lambda}{\gamma}$ where γ represents the pitch of the phase ramp and λ is the wavelength

[9]. The displacement d of the beam is therefore limited geometrically by the focal length of the lens used to focus the beam onto the target area according to the relation $d = f \tan \theta \approx f \theta$ for small values of θ .

When using the SLM to “steer” a focused spot in the context of reflective inverse diffusion, the only option currently available is selecting a new target area for focus and running through the optimization process as described in Section 3.6 for the new location. The limit to which the focused spot is steered to a given point is a function of the intensity of scattered light at the corresponding scatter angle. The fundamental geometric descriptor of reflectance is given by the bidirectional reflectance distribution function (BRDF) $f_r(\theta_i, \phi_i; \theta_s, \phi_s)$, describing the reflectance in a certain direction as specified by the angles defined in Figure 7. It is expected that the ability to “beam steer” is highly dependent on the BRDF of each particular sample. All steering experiments performed in this thesis are described in terms of these angles.

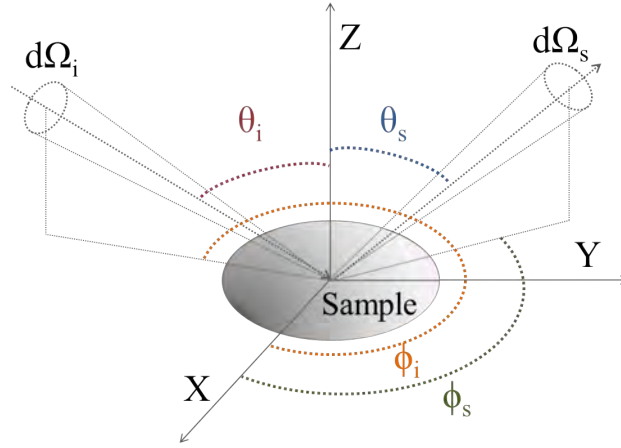


Figure 7. Schematic illustration of the bidirectional reflectance distribution function (BRDF).

The polar angle θ is measured from the surface normal while the azimuth angle ϕ is measured from an arbitrary reference in the surface plane [10]. For the current purpose, this reference is the plane containing the incident beam ($\phi_i = 0$).

2.7 Reflective Inverse Diffusion within Indirect Photography

To tie together the concepts which have been laid out, the progression for which reflective inverse diffusion will theoretically reduce indirect photography to dual photography while imaging components still have no line of sight to the object should be outlined. This thesis aims to provide a proof of concept for reflective inverse diffusion, demonstrate nonmechanical beam steering within the context provided in Section 3.9, and establish a framework by which enhancement can be predicted with knowledge of the scattering properties of various materials. The arrayed detector (AD) used to detect the target intensity currently takes the place of the hidden object.

The motivation to collocate the light source with the camera without a line of sight to the object is analogous to the motivation to provide feedback to the SLM from a detector which is collocated with the camera: the potential value of indirect photographing techniques lie with the ability to image an object which is hidden from all optical components which are used to image it. Figure 8 illustrates how introducing a second AD to record intensity pattern data serves first to establish a relationship between patterns of scatter at the target and at a location displaced from the target; the second AD subsequently uses the relationship to provide feedback to the SLM. Furthermore, this is done repeatedly until the AD which is gathering scatter information from the diffuse surface is collocated with the laser and the remainder of the imaging system.

2.8 Diffusely Reflecting Materials

Six reflectors are chosen based on the extreme variation of their scattering properties. The differences in the materials' bidirectional reflectance distribution functions, surface roughnesses, and their resulting achieved enhancement offer insight into po-

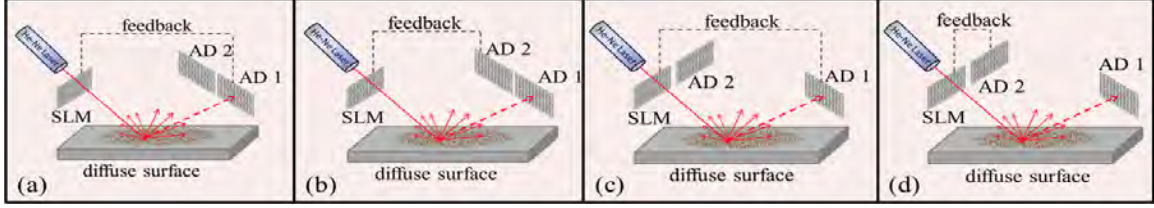


Figure 8. SLM feed back progression. To make reflective inverse diffusion useful in the context of indirect photography: (a) Gather intensity pattern information from another arrayed detector (AD) displaced from the focused spot and establish a relationship. (b) Establish a relationship between the intensity patterns and optimize using feedback from the second AD. (c) Repeat for greater displacements until (d) information gathered from an AD collocated with the laser can be used to control the SLM to achieve a focused spot on the first detector.

tential considerations in using this technique for indirect photography. The materials used include Spectralon, Infragold, a flat white paint sample, graphite, and two aluminum samples.

Spectralon is a translucent material consisting of sintered and compressed polytetrafluoroethylene. Its high reflectivity, low absorption, and nearly Lambertian radiative properties make it a useful radiometric calibration material in the infrared and visible spectra [11]. Infragold coating is another highly Lambertian material more commonly used in the infrared region of the spectrum for its excellent reflectance properties, but is also relatively reflective in the 632.8 nm region.

The white paint sample consists of a 0.25 mm silica cover slip with a thin layer of white spray paint, similar to the strongly scattering sample used in transmissive inverse diffusion. It is used to verify that the algorithm and equipment are set up correctly in a reproduction of Vellekoop’s experiment [3]. It is also used on reflection as another nearly Lambertian, highly scattering surface; however, with a layer of paint having a thickness on the order of $10 \pm 4 \mu\text{m}$, losses due to transmission decrease initial starting speckle intensity.

Graphite is a highly absorbing material in the visible region [12], and the two aluminum samples have significantly different surface roughnesses. One is lightly

brushed while the other is sandblasted, yielding two aluminum samples with differing BDRF's. The brushed sample has a stronger peak reflectance in the specular region as evidenced by its shine. Section 3.8 displays photos of all the samples.

2.9 Summary

Reflective inverse diffusion is a novel concept which is adapted from work done by Vellekoop *et al.* on transmission. Its potential use in reducing the complexity of indirect imaging to the imaging techniques applied in dual photography provides both the research motivation and the framework for determining a relevant geometric setup for experiments. The literature reviewed in this chapter provides background and context for the methodology presented in Chapter 3.

III. Methodology

3.1 Introduction

Using the background developed in Chapter 2, the methodology for this thesis is aimed towards providing a proof of concept for reflective inverse diffusion while operating in framework prescribed by the goal of its use in indirect photography. The optical setup outlined in Section 3.4 is used consistently for a set of diffusely reflecting materials with various scattering properties.

3.2 Laboratory Equipment

The main components of the laboratory setup include a 632.8 nm HeNe laser, Boulder Nonlinear Systems (BNS) LC SLM, and Santa Barbara Instruments Group (SBIG) camera. The reflective SLM has an array size of 7.68 mm by 7.68 mm consisting of 512 by 512 active pixels and a 2π phase stroke. The reflected wavefront distortion is $\lambda/15$, and the switching frequency is 30 Hz. The SBIG charged couple device (CCD) camera consists of 510 by 765 pixels which are each $9\text{ }\mu\text{m}$ by $9\text{ }\mu\text{m}$.

3.3 SLM Characterization

Per design, a pixel value of zero ideally results in maximum birefringence in the device while the strongest field and minimum birefringence occur with a pixel value of 255. The intermediate pixels would vary linearly from the minimum to the maximum value; however, LC molecular rotation does not vary linearly with applied voltage. Each SLM is shipped with a custom lookup table (LUT) to give an approximate mapping from pixel values to the voltages which will most closely result in a linear phase response. The phase response of the SLM should be measured to ensure the

appropriate set of pixel values is used to achieve the desired optical effect. BNS guarantees a linear phase response for a set of 50-100 pixels.

Fringe patterns are created using the Twyman-Green interferometer illustrated in Figure 9. The HeNe beam passes through a 50/50 non-polarizing beam splitter (NPBS), dividing the beam into one that illuminates the SLM and one that illuminates a reference mirror. The SLM and mirror are aligned so that they are nearly coplanar, and the beams interfere to form fringe patterns on the charge-coupled device (CCD) camera.

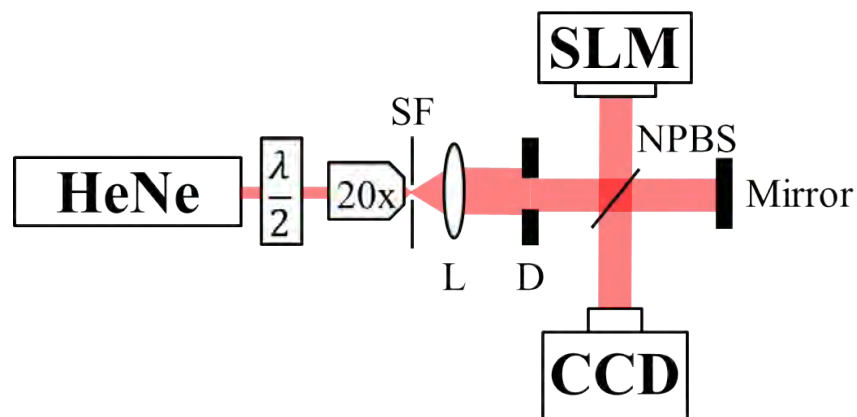


Figure 9. The Twyman-Green interferometer setup uses a half-wave plate, beam expanding spatial filter (SF), diaphragm (D), and non-polarizing beam splitter (NPBS). HeNe light from the SLM and mirror legs interfere to create patterns on the CCD.

Two techniques for measuring the phase response of the SLM are used to pinpoint the linear range of pixel addressability. In the first case, the phase response is measured by loading a matrix with all entries consisting of one constant grayscale value onto a large portion of the SLM for pixel values 0-255 while the remainder of the SLM is left to act as a mirror as depicted in Figure 10(a). The displacement of each fringe pattern for the modulated portion of the SLM is analyzed with respect to the unmodulated portion. In the second test, grayscale images consisting of alternating columns of zero value and values ranging from 0-255 are loaded onto the

SLM as shown in Figure 10(c) resulting in fringe patterns resembling the one shown in Figure 10(d).

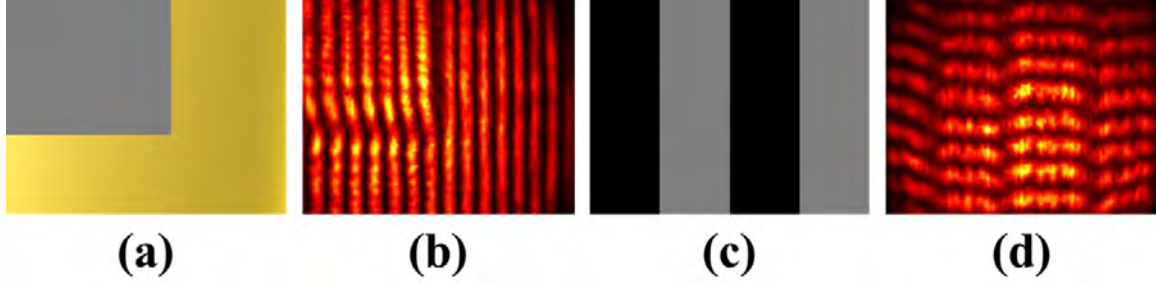


Figure 10. Calibration fringes (b) and (d) result from (a) constant gray scale values on a portion of the SLM, and (c) gray scale images with constant columns.

Averaging the recorded CCD intensity values over large portions of the resulting fringe patterns yields sinusoidal curves from which phase shift can be calculated straightforwardly with

$$\delta = 2\pi \left(\frac{\Delta}{\Lambda} \right) \quad (6)$$

where Δ is the displacement of the interference fringe peaks, and Λ is the period of the interference fringes [13]. Figure 11 displays the phase shift at each of the 256 pixel values for both techniques described, normalized so that the zero pixel value corresponds to a zero phase shift. While the absolute values for phase shift start to diverge as pixel values get higher for the two techniques, they have a similar overall shapes.

The two data sets are averaged and smoothed using a five-point averaging method to capture the underlying trend, and pixel values which mostly correspond to even increments of the maximum phase delay are recorded for use in the experiment. As a consequence, more of the pixel values used come from steeper segments of the curve.

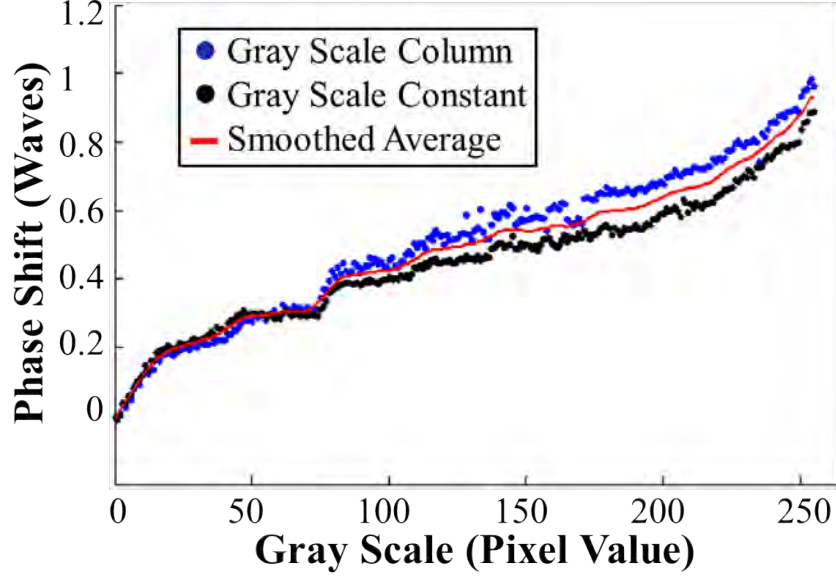


Figure 11. Phase response data. The data sets corresponding to alternating gray scale values and the application of a constant gray scale value to only part of the SLM yield similarly shaped trends. The smoothed average is used to pick out the pixel values giving even increments of the available phase delay range, which is about one wave.

3.4 Optical Setup

The setup used by Vellekoop for transmissive inverse diffusion, illustrated in Figure 12 involves a 632.8 nm HeNe laser beam expanded and reflected off of an LC SLM. Polarizers and quarter-wave plates are used for operation in a phase mostly modulation mode.

The primary experimental setup used for reflective inverse diffusion to achieve a focused reflected spot was designed to incorporate principles outlined by Vellekoop while keeping the goal of aiding in indirect photography in mind. Like the experiments described for indirect photography and transmissive inverse diffusion, a HeNe laser is used as the light source. As seen in Figure 13, the geometry of the setup is similar to that of transmissive inverse diffusion with the exceptions that (1) the SLM used is phase only so that polarizers are not needed, (2) the microscope objective which collects the scatter from the sample is removed for its impracticality with respect to

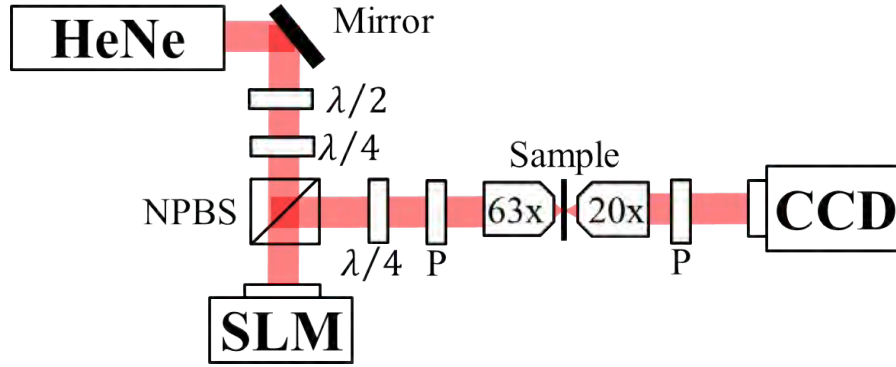


Figure 12. Transmissive inverse diffusion setup. A HeNe beam is expanded and reflected off an LC SLM. Polarization optics select a phase-mostly modulation mode. The SLM is imaged onto the entrance pupil of the first objective and focused onto the sample. The CCD camera images the transmitted intensity pattern.

indirect photography, and (3) the 63x objective was traded out for a lens (L2) with a focal length of 1 meter. Having an optical component so close to either side of the reflective sample would render reflective inverse diffusion trivial in the current context.

The 30-mW HeNe beam passes through a half-wave plate to orient its linear polarization with the slow axis of the phase only SLM. It is spatially filtered, expanded, collimated, and restricted to barely underfill the SLM before reflecting off of the mirror. While it is desirable to have a maximum number of phase modulating pixels available with which to work, overfilling the SLM would give rise to uncontrolled light reflecting off of the diffuse surface. The beam is split with an NPBS which dumps half the beam and transmits the other half for reflection off of the cover glass of the SLM. The beam is focused onto the reflective sample whose normal is oriented 45 degrees from the incoming beam. The camera is placed 40 ± 0.5 cm from the spot on the sample at 45 degrees on the other side of the surface normal so that it is centered on the specular region of the scattered reflection. All the reflective surfaces, detailed in Section 3.8, are highly scattering samples.

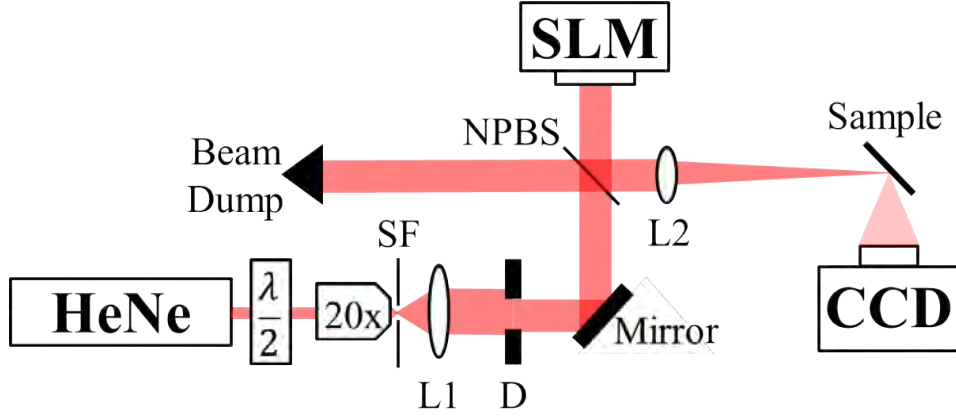


Figure 13. Reflective inverse diffusion setup. A 30 mW HeNe laser beam passes through a half-wave plate, is expanded (20x), spatially filtered (SF), and collimated (L1), and is restricted to the size of the SLM with a diaphragm (D). It is reflected off a mirror and divided with a non-polarizing beam splitter (NPBS). Half reflects off the SLM, split again, and focused (L2) onto the sample. The sample, which is oriented at 45 degrees with respect to both the incoming beam and the lensless camera (CCD), scatters the beam onto the detector.

3.5 Automated Experimental Control

A MATLAB routine was developed as the master program to control all components of the experimental setup. BNS supplied a MATLAB software development kit for manipulating the SLM in the form of a graphical user interface with options for preloading a set of phase screens. The provided code was modified to implement continuous downloading of phase screens as optimization was achieved. The SBIG CCD was controlled in MATLAB through calling a C++ executable file which was written and compiled in Visual Studio 2010. In a single iteration, a matrix of pixel values was loaded onto the SLM, the camera was called to capture an image with a 100-ms exposure time, the intensity values from the camera were read into MATLAB, the values from the target focus spot were summed, and the resulting target intensity provided an indication as to how to change the SLM input matrix for the subsequent iteration. Refer to Section 3.7 for a schematic outlining these operations and the time elapsed for each operation.

3.6 Phase Manipulation Algorithms

In the transmissive inverse diffusion case, there is a unique incident wavefront which makes the scattering material optimally focus light to a specific point. The wavefront is phase adjusted on the scale of the wavelength of light and cannot be constructed from a small set of smooth base functions, making efficient adaptive optics algorithms ineffective [6]. As a result, Vellekoop implements three algorithms which would solve for the phase solution by computational brute force.

The first is a stepwise sequential algorithm which varies one set of grouped pixels at a time to find and save the pixel value which leads to maximized target intensity on the detector, then loads all saved pixel values onto the SLM and cycles back through for another iteration. The second, depicted in Figure 14(c) and called the continuous sequential algorithm, is the same as the first except that the saved optimal pixel is loaded onto the SLM as it progresses to the next one. The final is a partitioning algorithm that randomly chooses half the grouped pixels, varies them as a set, and saves the optimal pixel value in the entire set; it is illustrated in Figure 14(b) [6].

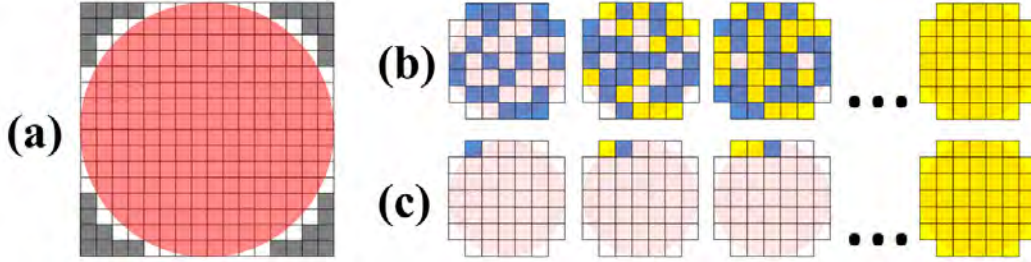


Figure 14. Pixel scheme. (a) SLM pixels which touch a diameter of 7.68 mm when the SLM face is divided into a grid of $N \times N$ grouped pixels are included in the optimization scheme. (b) Half the pixels are randomly chosen and optimized as a set. (c) One pixel is varied at a time and optimized pixel values are set as the algorithm runs.

The two algorithms depicted in Figure 14 are used in reflective inverse diffusion as a result of their reported performance results in transmissive inverse diffusion. In

every test presented, the partitioning algorithm starts achieving enhancement with the fewest iterations, and the continuous sequential algorithm achieves the highest overall enhancement by the end of each run. Figure 14(a) illustrates how only the SLM pixels for a given number of addressable segments, which the diameter of the laser touches, are varied in the algorithm while all remaining pixels in the corners are left at a zero setting. This ensures that run time is not wasted in attempting to optimize segments of the SLM which do not actually affect the beam.

The pixel radius of the target intensity region on the camera is set to the approximate size of a speckle for every test. For a given sample, speckle size is a function of the number of modulated segments used. A smaller segment corresponds to a larger number of total segments and a smaller speckle size on the detector. Chapter 4 includes an illustration of how speckle size varies when a random phase map of size $N=2$ to $N=64$ is loaded on the SLM for a given sample and optical configuration. Especially in a transition from one set of segments to the next, the speckle size will vary as optimization is taking place. To account for variations in the speckle size for a given number of segments, more weight is assigned to a pixel intensity value located at the center. The result is a bulls eye pattern of weighted target intensities as depicted in Figure 15.

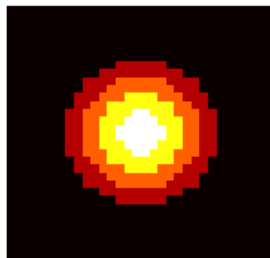


Figure 15. Target intensity weighting. The target area on the detector is assigned a weight based on its proximity to the center. The most highly weighted values are at the center (white) and decrease toward the edge (red).

Vellekoop suggests that minimizing the effect of noise can be accomplished through coarse pre-optimization [14]. To that end, the algorithm runs with small sets of large grouped pixels before decreasing grouped pixel size according to Figure 16. Chapter 4 opens with the results of a test which compare the enhancement achieved when a phase screen of a particular dimension N is applied with and without optimizing with the preceding smaller dimension N .

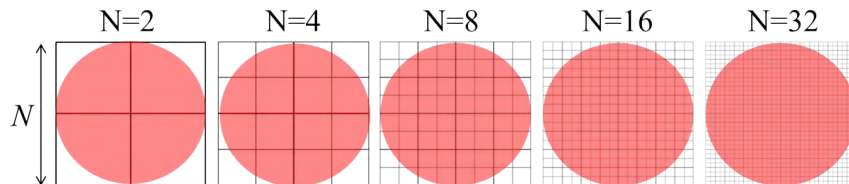


Figure 16. Grouped pixel dimensions. For a given reflector, the algorithm runs through increasing grouped pixel dimension size N , from $N = 2$ to $N = 32$.

3.7 System Limitations

The most notable limitations of the system developed to demonstrate reflective inverse diffusion center on the speed at which the solution space is searched for a phase map to bring the scatter to a focused spot. Figure 17 outlines the process by which the target area is optimized and the time it takes for each operation in the process. Since the camera is opened and closed to take a single frame of data between each iteration of the SLM being loaded with a particular phase screen, the maximum designed refresh rate of the SLM far exceeds the refresh rate required by the algorithm with each load.

A single test running from $N = 2$ to $N = 32$ involves the optimization of a total of 1160 individual pixels. Each pixel requires an image be taken for a given phase value. If the phase step $\Delta\phi$ is set to $\pi/10$, each pixel must run through 21 values for optimization. The test thus takes a little over ten hours to run through a set for a

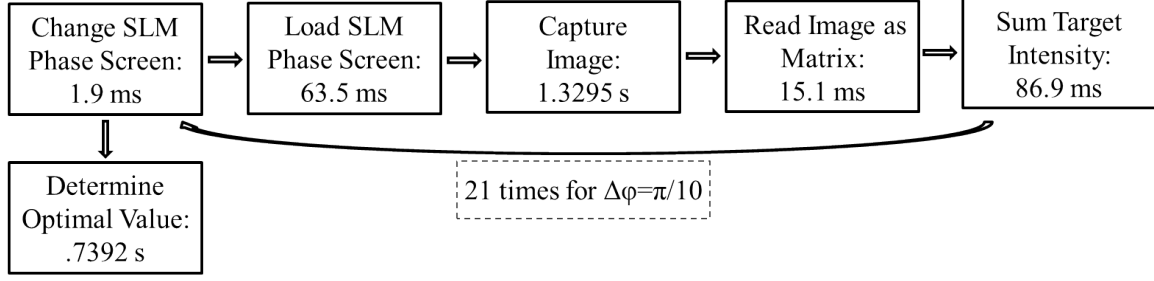


Figure 17. Algorithm schematic for one grouped SLM pixel. To take a single measurement, the listed algorithm takes approximately 1.5 seconds. For a stepsize $\Delta\Phi = \frac{\pi}{10}$, a grouped pixel is optimized in around 32 seconds.

single sample. Section 5.4 offers suggestions for how to improve upon the algorithm laid out here in order to achieve the desired enhancement with significantly less run time.

3.8 Reflection Materials

The six diffuse reflectors used to demonstrate reflective inverse diffusion include Spectralon, a dull aluminum sample, a slightly polished aluminum sample, Infragold, a glass cover slip covered with a thin layer of white paint, and a block of graphite. Figure 18 displays photos of the samples.

Profilometer measurements are taken with a Tencor Alpha Step 1000 Surface Profiler for each of the samples used in reflective inverse diffusion. A single scan lasts 8.5 minutes while covering a distance on the surface of 1 mm. These 10 nm resolution scans are included in Appendix C, and their corresponding RMS optical surface roughnesses are calculated with

$$\sigma = \sqrt{\left(\frac{1}{L}\right) \int_0^L ((z(x) - \bar{z})^2 dx} \quad (7)$$

where L is the length of the scan and $z(x)$ is the surface height as a function of position x [15].

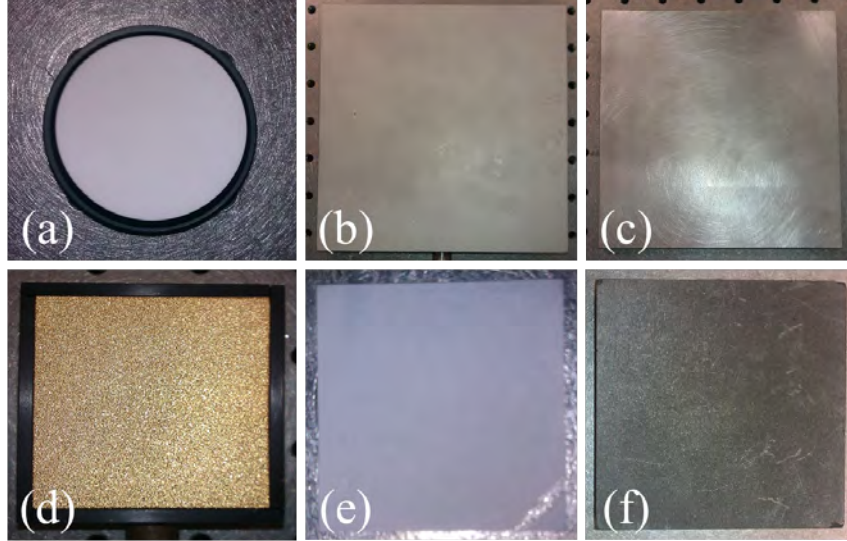


Figure 18. Reflective surfaces. Reflective inverse diffusion is performed on and compared for (a) Spectralon, (b) unpolished aluminum, (c) slightly polished aluminum, (d) Infragold, (e) white paint on a glass cover slip, and (f) graphite.

The target focus for each sample is aligned with the center of the specular region of reflection. The method used for alignment involves starting with a mirror turned to 45 degrees from the incident beam and setting up a fast lens to focus in the direction of the camera. The camera is translated until the spot is focused at its center. The diffusely reflecting surface is inserted and rotated to 45 degrees, then translated until the scattered focus is centered on the camera, and the lens is removed. The process is repeated for each sample because the mounts and reflector thicknesses vary from sample to sample. The entire setup is covered with black cardboard and black felt to shield all optical components from air currents and external reflective surfaces.

3.9 Nonmechanical Beam Steering

Nonmechanical beam steering in the context of reflective inverse diffusion is demonstrated with three basic experiments. The first involves consecutively optimizing to a spot in each corner of the CCD without moving anything in the setup using the

white paint reflector. The second and third require the translation of the camera from regions of specular reflection to regions of diffuse reflection. Figure 19 illustrates the simulation of the scanning of a playing card off of the polished aluminum sample. The specular region is considered the starting point on the upper left corner of the card. The camera is translated in two dimensions so that the distance from the sample to each side of the simulated playing card is fixed at 40 ± 0.25 cm.

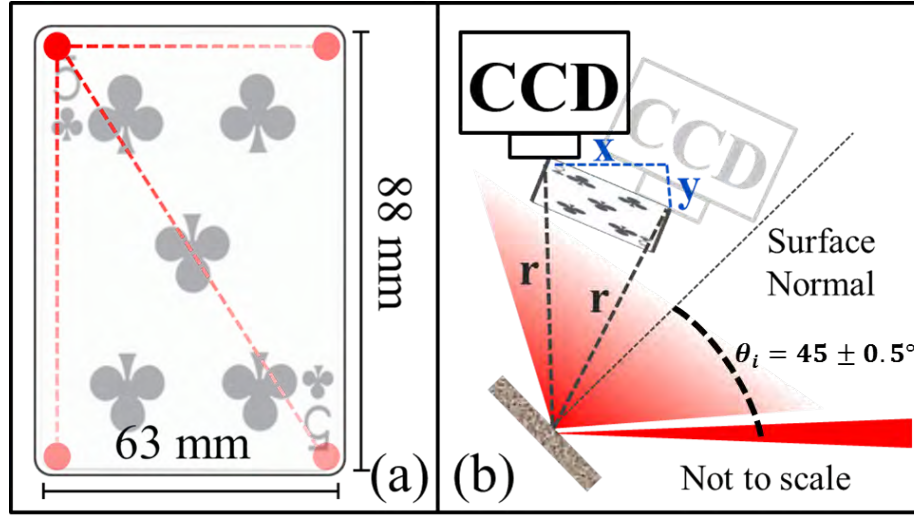


Figure 19. Beam steering across playing card. (a) The top left corner is set to the specular reflection region of the scatter. (b) The camera is translated so that the detector corresponds to the corner points of the playing card while keeping the distance between the reflector and the CCD at 40 ± 0.25 cm.

To test the extent of the ability to focus the diffuse scatter from each of the samples, the camera is placed 40 ± 0.25 cm from the reflector in the plane of incidence. This corresponds to an incident angle of 45 ± 0.5 degrees as before, and a scattering angle of 0 ± 0.5 degrees.

3.10 Speckle Pattern Decorrelation Test

Quantification of the decorrelation of the speckle pattern is achieved with an experiment which mimics the operations involved in inverse diffusion. As illustrated in Figure 20, the algorithm generates and loads a random phase screen of a certain dimension N . The phase screen is saved as a reference phase screen, and the corresponding image of the speckle pattern on the detector is saved as the reference image. Random phase screens are generated and applied to the SLM, but their corresponding detector images are not saved. The algorithm periodically returns to the reference phase screen, and the corresponding image is saved. The time at which the reference phase screen is reloaded is stored.

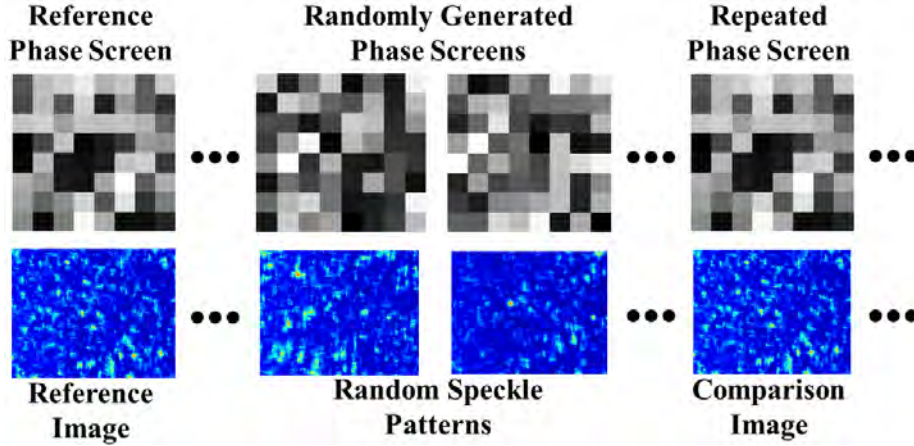


Figure 20. Speckle decorrelation test. A phase map of a certain dimension N is randomly generated and saved as the reference SLM while its corresponding speckle pattern on the AD is saved as a reference image. The algorithm continues to load randomly generated phase maps and periodically returns to the reference phase map. The speckle patterns which correspond to the reference phase map are recorded for comparison with the initial recorded speckle pattern.

The correlation coefficient is the metric used for assessing the similarity between the reference image and subsequent images resulting from the same applied phase screen. Comparing two images pixel by pixel and calculating the covariance divided by the product of their respective standard deviations, the coefficient is given by

$$r = \frac{\sum_m \sum_n (A_{mn} - \bar{A}) (B_{mn} - \bar{B})}{\sqrt{\left(\sum_m \sum_n (A_{mn} - \bar{A})^2\right) \left(\sum_m \sum_n (B_{mn} - \bar{B})^2\right)}} \quad (8)$$

where A corresponds to the reference image matrix of intensity values, B corresponds to the subsequent image matrix, the subscript m denotes the pixel row, and the subscript n denotes the pixel column.

3.11 Summary

The experiments presented in this thesis aim to provide a proof of concept for adapting transmissive inverse diffusion to the case of reflection, particularly in geometric setups which are practical within the context of indirect photography. The SLM is characterized for use in experiments involving optimization to achieve enhancement in the specular and diffuse regions of scatter reflected from six samples. The same algorithm is applied on transmission for comparison to the literature presented in Chapter 2. The results attained using the methodology given in this chapter are presented and analyzed in Chapter 4.

IV. Results and Analysis

4.1 Introduction

The results outlined in this chapter include the reproduction of the technique used by Vellekoop in focusing light transmitted through a thin white paint sample. These measurements serve as a baseline with which to compare results achieved on reflection for the same thin paint sample along with the brushed aluminum, sand-blasted aluminum, graphite, spectralon, and infragold reflectors. For every reflector, enhancement achieved for the specular region is further compared to increasingly diffuse regions of scatter in order to evaluate the potential for steering the focused spot. This chapter also provides insight into aspects of the setup and technique which most affect the results for each experiment.

4.2 Optimization Considerations

Tests are performed using both the pre-optimization scheme outlined in Section 3.6 and without pre-optimization to ensure that the extra time used to optimize smaller values for N increases rather than decreases algorithm efficiency. Figure 21 displays the results for a set of runs in which two factors are varied for the graphite sample. In the test denoted by the solid magenta line, the phase modulation step size is the smallest to achieve greater SLM phase resolution, and the optimization for each dimension occurs after being pre-optimized by the dimension preceding it. In the test denoted by the blue dashed line, the phase modulation step size is reduced, but it still undergoes pre-optimization for each dimension. In the final test given by the black dotted line, the phase modulation step size is reduced by the same amount as in the preceding test, but the optimization for each dimension stands alone without pre-optimization.

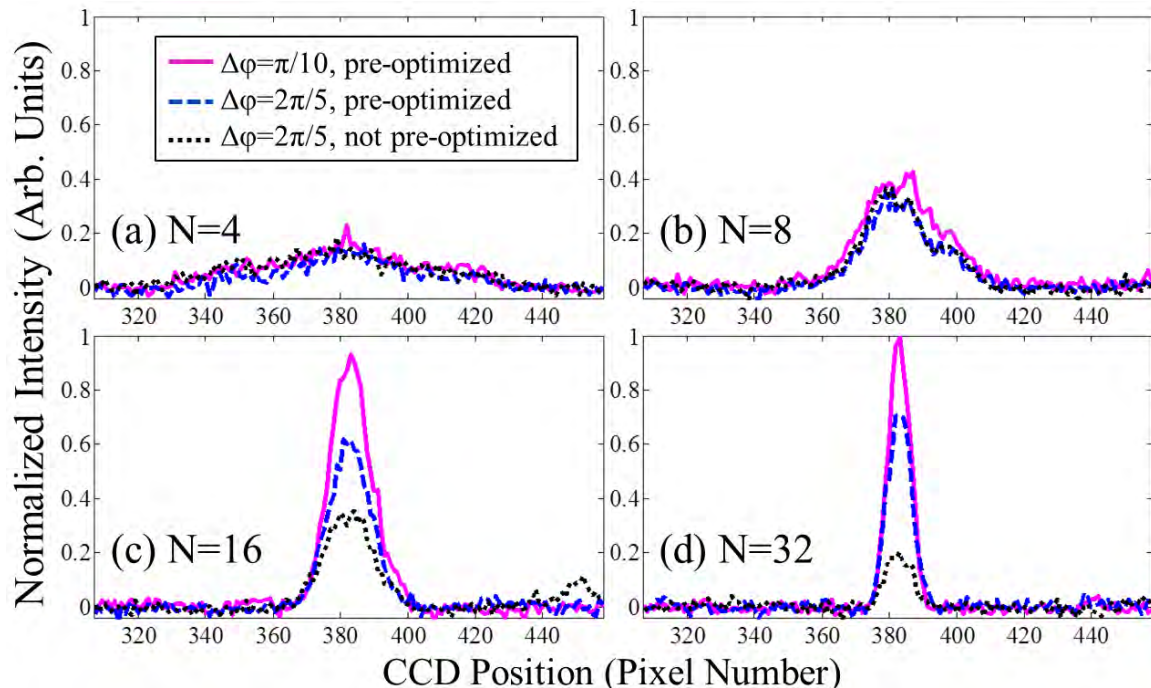


Figure 21. Pre-optimizing the SLM. Intensity profiles cut through the center row of the AD are shown for the optimization of reflection off of graphite for pre-optimized runs and runs that are not pre-optimized. Pre-optimizing the SLM and decreasing the phase delay step size $\Delta\phi$ show higher relative intensity of the optimized spot. The plots come from the final intensity profiles for the (a) $N = 4$, (b) $N = 8$, (c) $N = 16$, and (d) $N = 18$ optimization schemes.

Performance of the algorithm is similar for all cases for dimensions $N = 4$ and $N = 8$. The peak intensities start diverging for $N = 16$, and peak intensity actually decreases from the $N = 16$ to the $N = 32$ stage for $\Delta\Phi = 2\pi/5$ without pre-optimization. As a consequence of these results, all experiments run from $N = 2$ to $N = 32$ consecutively using the higher resolution phase step. An added advantage of running through each size N is the ability to pinpoint the phase screen dimension for which the optimization breaks down for a particular sample with a single run.

For transmissive inverse diffusion, Vellekoop reported that the target intensity responds sinusoidally when changing the phase of one or more segments on the SLM. The wave is sampled by taking ten measurements and fitting a curve which exploits the entire range of available phase delay [3]. For reflective inverse diffusion, the current

setup does not consistently yield a sinusoidal response in target intensity as a function of phase delay. As shown in Figure 22, the target intensity variation from infragold scatter appears roughly sinusoidal for $N = 4$ and $N = 8$, but varies randomly for the other stages. All samples exhibit similar target intensity behavior.

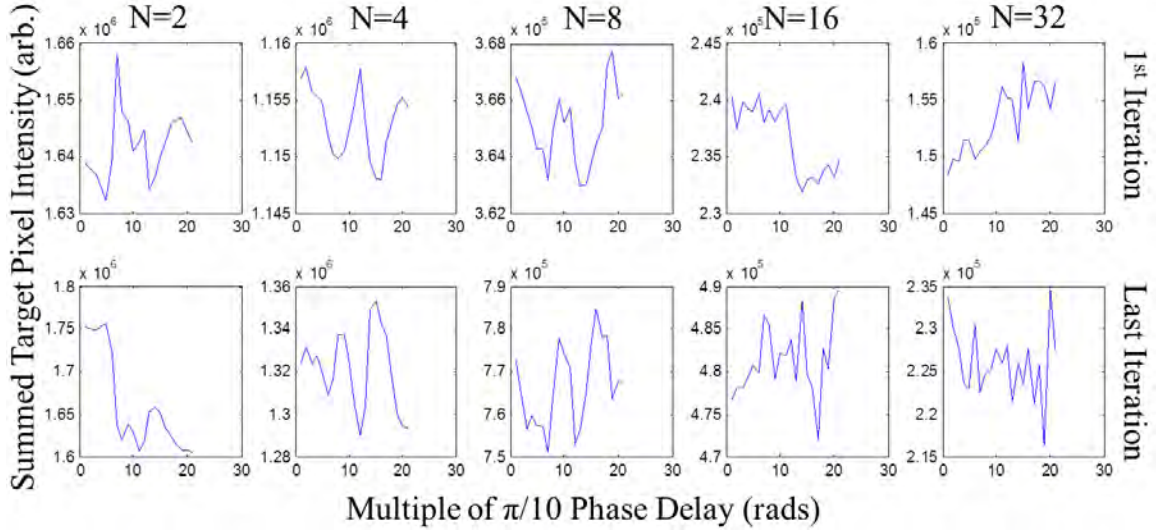


Figure 22. Target intensity variation with phase delay. The summed target intensity values for infragold show a roughly sinusoidal pattern for $N = 4$ and $N = 8$ while the $N = 2$, $N = 16$, and $N = 32$ have dissimilar amplitudes and periods.

As a result, the optimization scheme used in this thesis is not able to achieve the resolution used by Vellekoop in selecting the phase delay which optimizes a particular pixel on the SLM. While the algorithm takes twice as many measurements, the the algorithm used by Vellekoop further fits the intensity response values from the detector to a curve given by

$$I(\Phi) = I_A + I_B + 2\sqrt{I_A I_B} \cos(\Phi - \Phi_0) \quad (9)$$

where I_B is the intensity at the target from the modulated segments, I_A is the target intensity caused by light from the other segments, Φ is the varied phase, and Φ_0 is the unknown optimal phase value for the current segment. Vellekoop is therefore able

to assign pixel values corresponding to the entire range of available hardware-limited SLM phase delay.

4.3 Speckle Size

Without using a lens to collect the light scattered from the diffuse surface, control of the speckle size on the detector is limited for a given geometry. Figure 23 illustrates how with varying only the value N on the SLM, the speckle size changes significantly. In this case, the sandblasted aluminum reflector produced the interference patterns shown on the detectors for randomly generated phase maps with $N = 2$, $N = 4$, $N = 8$, $N = 16$, and $N = 32$. All samples show similar variation in speckle pattern size.

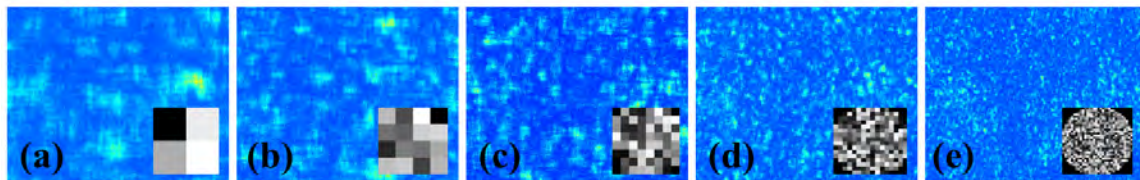


Figure 23. Speckle size varies with N . Without altering the geometry of the setup, applying random phase maps with (a) $N = 2$, (b) $N = 4$, (c) $N = 8$, (d) $N = 16$, and (e) $N = 32$ leads to significant differences in the speckle size of the interference pattern on the detector. The patterns displayed here are from the dull aluminum reflector.

As mentioned in Section 2.4, the final enhanced spot is given by the constructive interference of the speckle patterns of the individually phased beams. Section refsec-SSA relates the sizes of the enhanced spots described in the following sections to the dimensions of the phase screens used to formulate them.

4.4 Comparison of Reflective Surfaces

Table 1 outlines the performance of the optimization technique for each of the reflectors along with its measured surface roughness R_{rms} and the full width at half

maximum of the final focused spot. The spot is evaluated using Vellekoop’s definition of enhancement in Equation (4). It is calculated by picking out the pixels of the detector that fall within the full width at half maximum (FWHM) of the target focus and computing the collection’s RMS value with respect to the mean of the surrounding speckle pattern. The enhancement is the ratio of this RMS value to the RMS value of the surrounding speckle pattern at a radius of three times the FWHM and outward.

Table 1. Specular Enhancement.

Reflective Samples	Enhancement (η_R)	Roughness (R_{rms})	Final FWHM
Brushed aluminum	122.3	$1.5\mu\text{m}$	$36\pm 3\mu\text{m}$
Infragold	89.9	$9.4\mu\text{m}$	$38\pm 3\mu\text{m}$
Sandblasted aluminum	67.7	$2.3\mu\text{m}$	$38\pm 3\mu\text{m}$
Graphite	37.3	$3.5\mu\text{m}$	$41\pm 3\mu\text{m}$
White paint	36.8	$1.7\mu\text{m}$	$41\pm 3\mu\text{m}$
Spectralon	13.8	Unprofiled	$45\pm 3\mu\text{m}$
Transmissive Sample			
White paint	56.4	$1.7\mu\text{m}$	$63\pm 3\mu\text{m}$

The enhancement as a function of the pixel optimization iteration from the $N = 2$ through the $N = 32$ cases are shown in Figure 24 with the $N = 16$ and $N = 32$ portions highlighted in gray and yellow, respectively. Enhancement for every reflector increases most rapidly for the $N=16$ optimization stage and either decreases or levels off during the beginning of the $N = 32$ stage. Graphite and Spectralon show no improvement during the $N = 32$ stage, and white paint shows little improvement before the enhancement decreases again to a value slightly above its enhancement for $N = 16$. The primary factor attributed to the lack of enhancement achieved for these three samples is the signal-to-noise ratio (SNR) of the speckle pattern for increasing SLM dimension N .

A second factor which leads to further decrease in enhancement for Spectralon as the algorithm progresses for $N = 32$ is the rate at which the speckle pattern

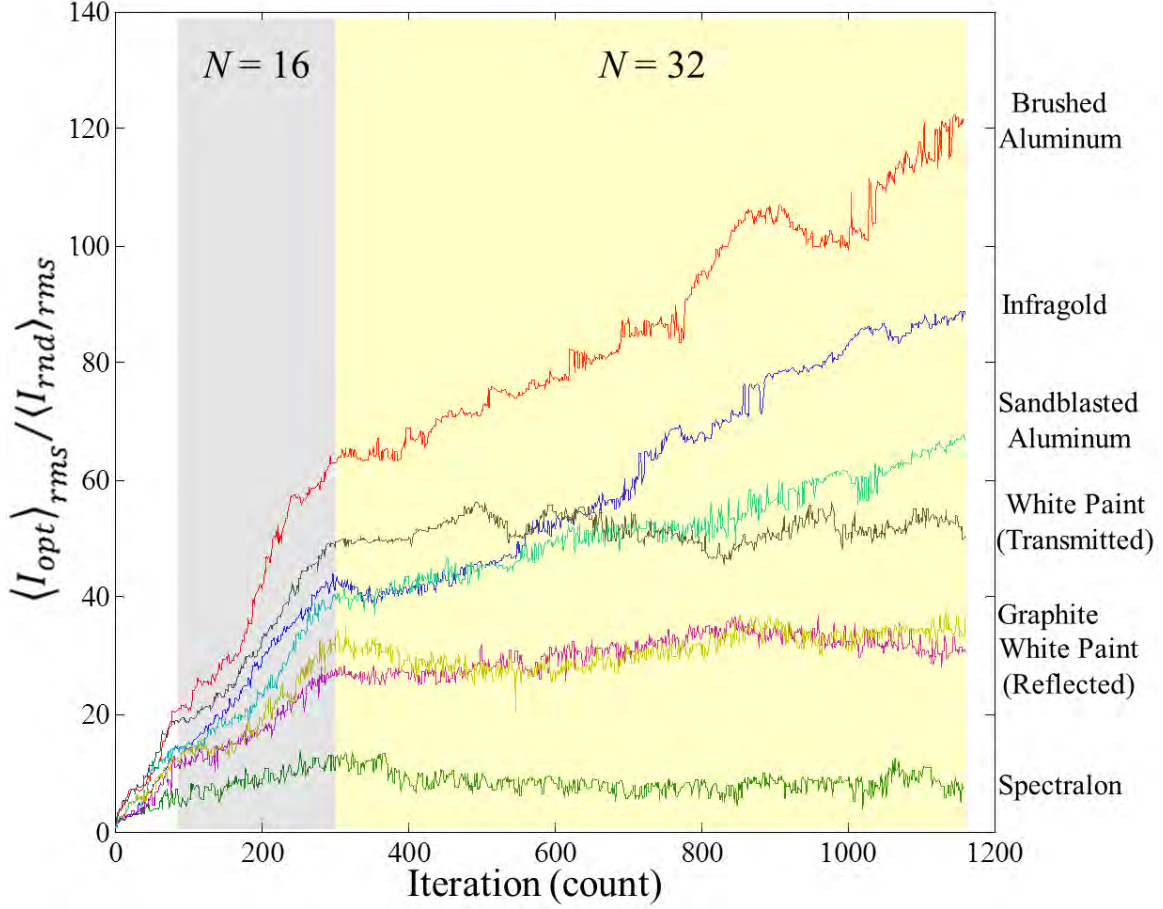


Figure 24. Sample enhancement comparison. The enhancement η_R as defined in Section 2.4 is plotted as a function of the optimized pixel iteration for SLM dimension $N = 2$ through $N = 32$. The $N = 16$ iterations are highlighted in gray while the $N = 32$ iterations are highlighted in yellow.

decorrelates. Given its translucent properties mentioned in Chapter 2, light enters the sample and undergoes multiple scattering before it reemerges. Recent experiments involving the determination of the penetration depth for HeNe light in samples of Spectralon have produced estimates of around $200\mu\text{m}$ [16]. This value is around 20 times the thickness of the white paint sample, indicating that the shaped HeNe beam undergoes many more scattering events upon reflection within the Spectralon sample than through the white paint sample on transmission. A specific illustration of the decorrelation of the Spectralon speckle pattern on reflection and the white

paint sample speckle pattern on transmission as a function of time is shown explicitly in Section 4.7.

The brushed aluminum reflector yielded the highest enhancement of the set. Figure 25(a) shows the intensity ratios between the final images for each phase map pixel dimension N and the average starting speckle pattern for that N . Random phase maps for a particular size N are applied to determine a starting intensity value to which the images and plots are normalized. The speckle patterns are displayed using a logarithmic scale in order to capture the intensity distribution around the focused spot. See Appendix D for similar displays of the other reflecting surfaces.

Figure 25(b) shows the same information for the optimization process for the white paint sample on transmission. The speckle size remains fairly constant as the SLM dimension size N is increased. The optimization algorithm fails to increase the enhancement for the sample for the $N = 32$ stage due to the decorrelation of the speckle pattern. The $N = 32$ curve shows a smearing out of the optimized spot in spite of a consistent background speckle size. This can be thought of as the individual speckle patterns each decorrelating to smear out the effect of their constructive interference at the target.

4.5 Spot Size Analysis

The varying speckle size observed in Section 4.3 leads to corresponding variations in the final focused spot size for each SLM dimension N . The relationships which govern these variations come from considering the light propagating from a given pixel as an individual beam and applying Fraunhofer diffraction theory. Figure 26 illustrates the relevant quantities.

The spot diameters q_1 and q_2 on the reflective surface and on the detector, respectively, go as

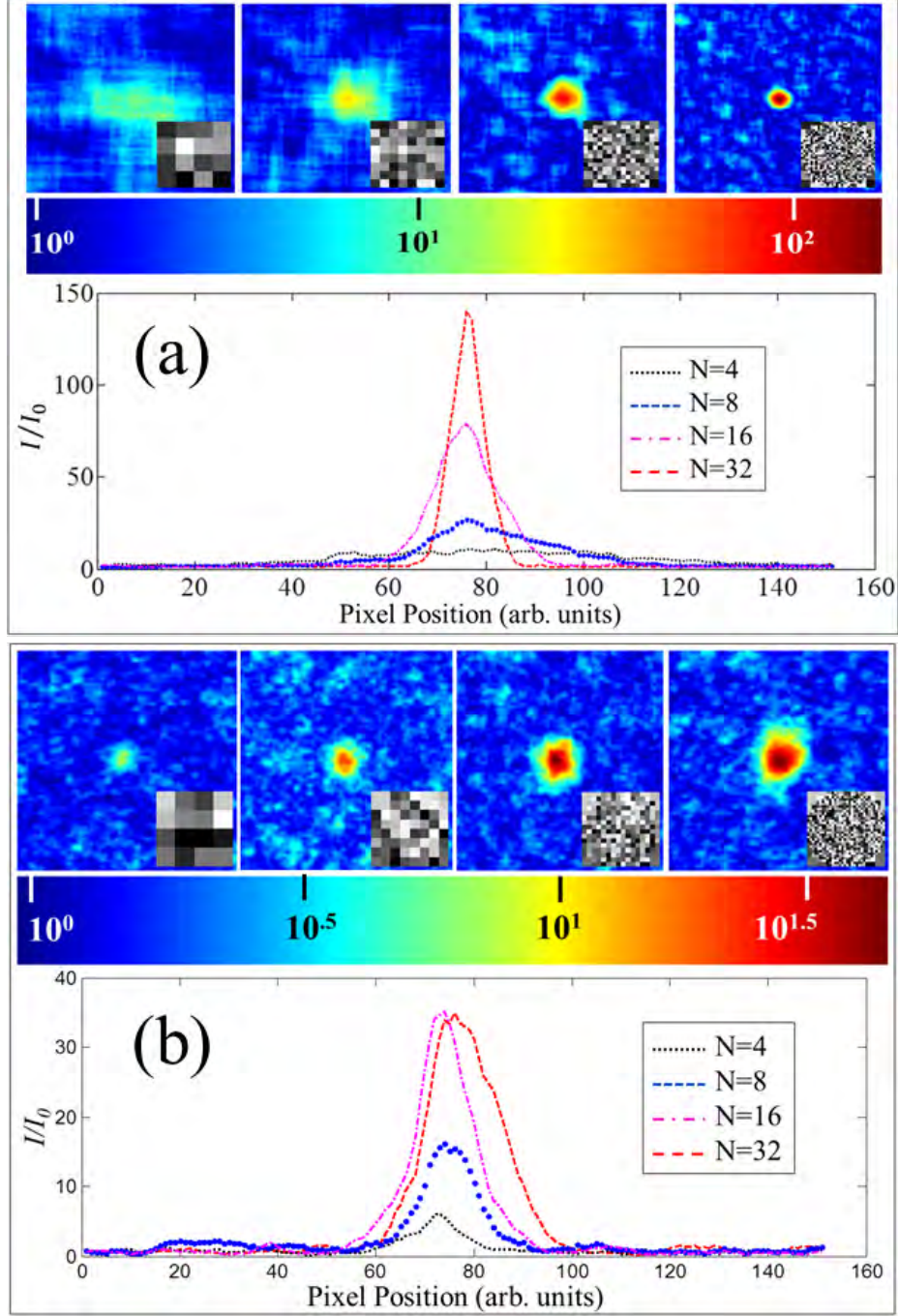


Figure 25. Sample relative intensity comparison. The top half of each block displays the interference pattern from a portion of the detector center for phase screens of $N = 4$, $N = 8$, $N = 16$, and $N = 32$. The pattern is normalized to the average starting intensities and plotted on a logarithmic scale. An image of the corresponding phase screen applied is shown with a phase delay of zero corresponding to black and a phase delay of 2π corresponding to white. The bottom half of each block shows the center row of intensity values recorded from the detector on the final image of each SLM dimension optimization. This data is displayed for (a) brushed aluminum on reflection and (b) white paint on transmission.

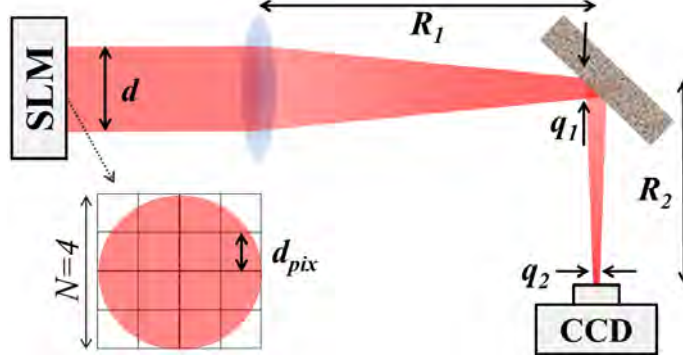


Figure 26. Spot size relationships. The spot size on the sample q_1 is a function of the grouped pixel size d_{pix} . This in turn affects the size of the enhanced spot q_2 recorded on the detector.

$$q_1 \sim \frac{\lambda R_1}{d_{pix}} \quad (10)$$

and

$$q_2 \sim \frac{\lambda R_2}{q_1}. \quad (11)$$

Substituting for d_{pix} and simplifying, the final relationship becomes

$$q_2 \approx \frac{R_2}{R_1} \frac{d}{N}. \quad (12)$$

Considering that $R_1 \approx f$, the lens focal length, geometry of the setup, and the pixel dimension are the primary factors in predicting the spot size of the enhanced spot on the detector.

In order to extract the boundaries of the focused spot from the background of random speckle and noise, a 1-dimensional autocorrelation is applied to the center row of intensity values from the AD. The original intensity distribution as a function of x is displaced by an amount ϵ . Displacing the function a pixel at a time, the area under the product of the displaced and undisplaced versions of the distribution give the degree of overlap in accordance with

$$c_{ff}(\epsilon) \equiv \int_{-\infty}^{+\infty} f(x + \epsilon) f^*(x) dx. \quad (13)$$

The function $f^*(x)$ denotes the complex conjugate of $f(x)$.

Figure 27 displays the autocorrelations performed for every reflective sample for the final optimization iteration corresponding to $N = 8$, $N = 16$, and $N = 32$. The distance between $\epsilon = 0$ and the point at which the autocorrelation values start leveling off into a baseline noise value gives the full width of the enhanced spot. The vertical lines point to the values of the predicted spot size (red center lines) and the uncertainty bounds (cyan and purple outer lines). The autocorrelations show similar spot sizes for each pixel dimension for all six reflective samples and are in good agreement with the predicted values of $384 \mu\text{m}$ for $N = 8$, $192 \mu\text{m}$ for $N = 16$, and $96 \mu\text{m}$ for $N = 32$.

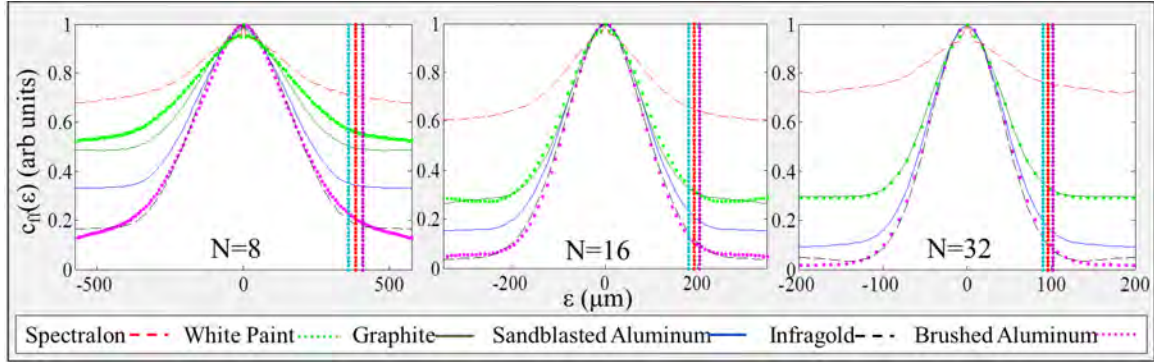


Figure 27. Signal autocorrelation. The autocorrelation is shown for each sample for SLM dimensions $N = 8$ through $N = 32$. The vertical bands denote the predicted value (red center line) with uncertainty bounds (cyan and purple lines) of the spot diameter. The point at which the autocorrelation levels out corresponds to the edge of the focused spot.

4.6 Nonmechanical Beam Steering

As mentioned in Chapter 2, nonmechanical beam steering is typically thought of as a technique to steer a coherent beam effectively using a phase screen as a diffraction

grating. In the context of reflective inverse diffusion, nonmechanical beam steering is equivalently the ability to choose a displaced target area to overlay speckle patterns of individually modulated segments of the beam and achieve a focused spot. The first demonstration of beam steering involves choosing the four corners of the CCD to optimize reflection from the white paint sample using $N = 2$ to $N = 16$. The optimization algorithm for each spot is the same as that outlined in Section 3.6, except that it does not progress through the $N = 32$ stage, and the algorithm runs four times consecutively with target areas defined in one of the four corners instead of the center. Figure 28 shows the four final iteration images using the same logarithmic scaling and normalization to the average starting intensity as is used in Figure 25.

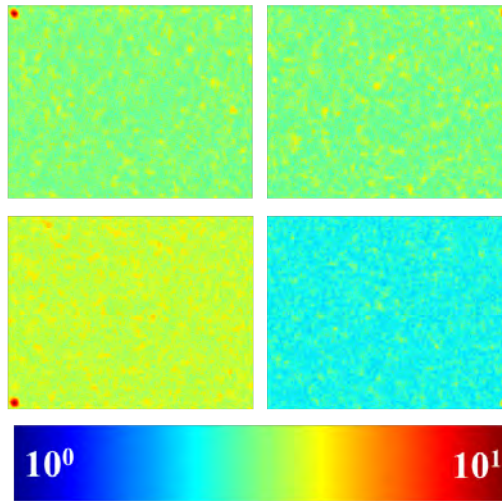


Figure 28. Beam steering to CCD corners. Continuous runs from $N = 2$ to $N = 16$ are performed on the white paint sample for the four corners of the CCD to illustrate how the detector can be scanned without moving anything in the setup.

As expected, all spots show similar peak intensity values. They are separated lengthwise by 6.9 mm, 4.6 mm vertically, and 8.3 mm diagonally. This corresponds to a steer angle of 31.3 mrad with respect to the scattering surface. The peak intensity of the least enhanced spot on the CCD is within 13.5% of that of the most highly enhanced spot.

Steering across the face of a playing card requires a beam displacement of 88 mm vertically, 63 mm horizontally, and 108.2 mm diagonally. Figure 29 displays the intensity profile slices corresponding to spots at each of these corners as described in Section 3.9 for polished aluminum. The plots are arranged in the figure according to their locations on a the face of a playing card; i.e., the top left plot corresponds to the top left corner of the card, etc. Enhancement decreases by 58.6% with the diagonal distance from the top left specular region of the card to the bottom right region. The reduction in enhancement is smaller than the plotted reduction in peak intensity because the enhancement is the ratio of the RMS focus intensity to the surrounding speckle pattern, and the RMS intensity of the surrounding speckle pattern for the specular region of the playing card is greater than for the diffuse region.

To compare the extent of beam steering capabilities and to allow for comparison across all samples, the CCD is moved to fall in line with the surface normal, corresponding to an incident angle of 45 ± 0.5 degrees and a scattering angle of 0 ± 0.5 degrees. Figure 30 shows the enhancement as a function of pixel optimization iteration for each of the six samples. Both the specular reflection enhancement and the diffuse reflection enhancement are plotted.

For all samples, the test runs through $N = 2$ to $N = 16$. Polished aluminum, the reflector which yielded the highest specular reflection enhancement, achieved negligible enhancement in the more diffuse region of its scatter due to its overwhelming concentration of specular reflection. The sandblasted aluminum and infragold enhancements in the direction of the surface normal reached 45.40% and 40.04% of their specular enhancements, respectively.

Spectralon, a highly Lambertian, reflective sample with a short persistence time performed nearly equivalently for both specular and diffuse enhancement. Graphite, a good absorber in the visible spectrum, showed negligible enhancement in the diffuse

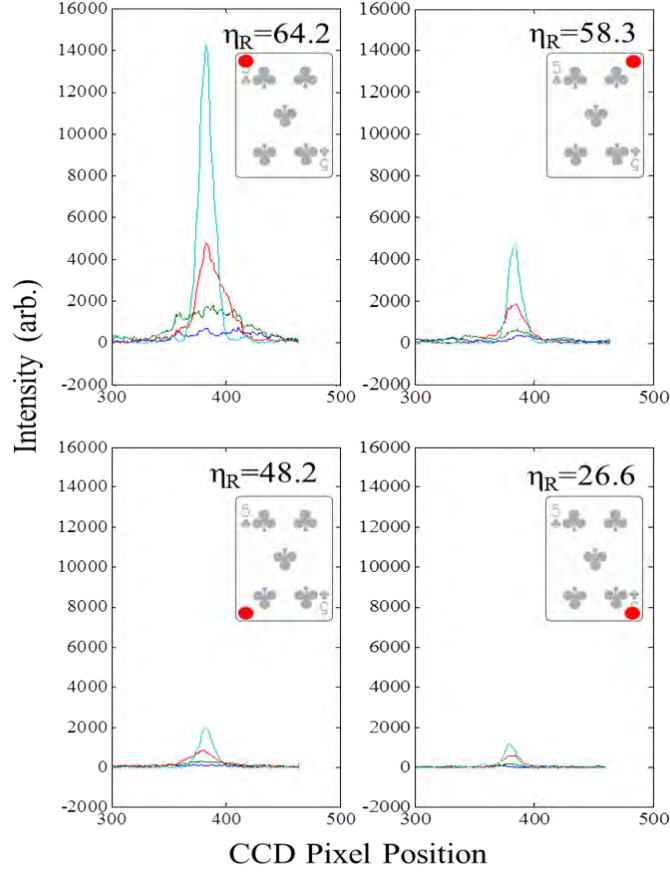


Figure 29. Beam steering along dimensions of a playing card. The polished aluminum reflector is used to illustrate the decrease in enhancement for spots corresponding to the corners of a playing card. The top left corner, the optimization target which lies in the specular region of reflection, achieves the highest enhancement. Enhancement falls off with distance from the specular region.

region. Noted earlier for its loss due to transmission, the white paint sample showed little enhancement in the diffuse region, as well.

For high displacement beam steering, the samples which are both strongly scattering and highly reflective tend to achieve enhancements more comparable to their respective specular enhancements. The use of nonmechanical beam steering is thus limited by the intensity of light reflected at various scatter angles. In the context of indirect photography, for which an object is potentially scanned with a focused beam using reflective inverse diffusion, the scattering properties of diffuse materials become

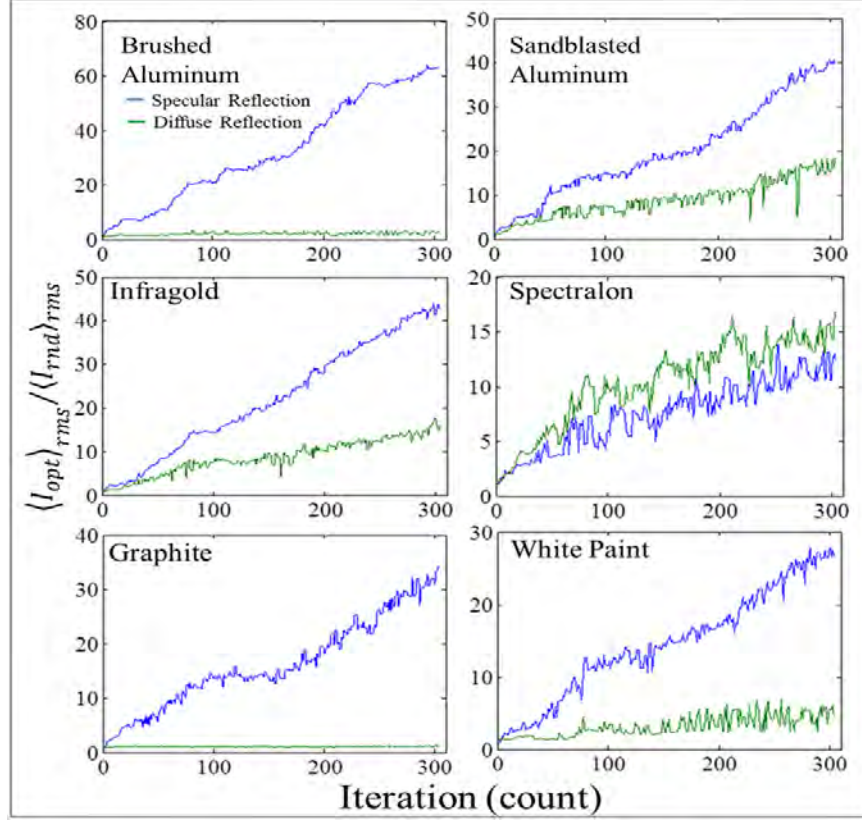


Figure 30. Enhancement comparison of specular to diffuse reflection. Enhancement is plotted as a function of the optimization iteration for each sample with the camera placed in the specular region of reflection (blue) and at a scatter angle of 0 ± 0.5 degrees (green).

an aid rather than a hindrance for objects extending outside of the specular region of scatter.

4.7 Speckle Pattern Decorrelation

Further exploration of the speckle pattern decorrelation shows trends which vary from sample to sample. Correlation coefficients between a reference image of the speckle pattern for a particular sample to subsequent images of the speckle pattern are computed as outlined in Section 3.10. Plotting these coefficients as a function of the time which passes between the reference image and the comparison images being taken gives rise to Figure 31.

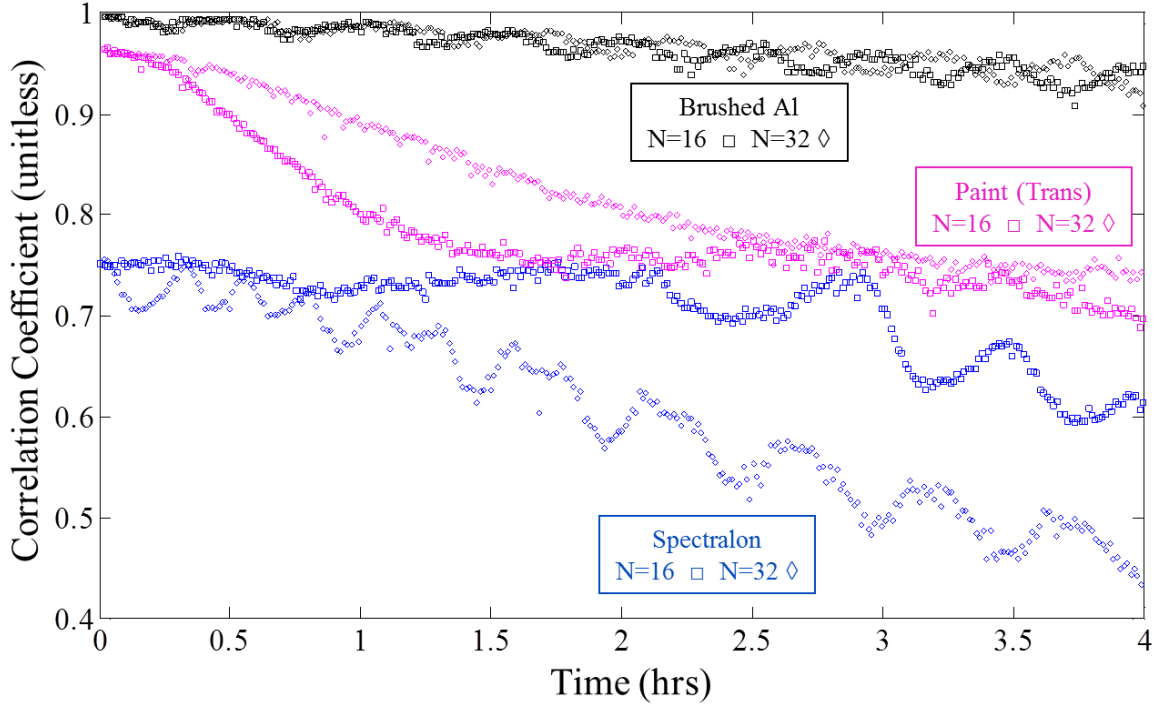


Figure 31. Speckle decorrelation. Images taken for a particular phase screen are compared to the initial reference image using the correlation coefficient, and the coefficients are plotted as a function of time.

It should be noted that the displayed results of the decorrelation test are dependent on both the properties of the material and the environmental conditions for each individual test. The oscillatory nature of some of the data suggests that certain periodic perturbations exist within the setup, e.g. fluctuations in detector fan speed, laser output power, or laboratory HVAC. Section 5.4.2 offers suggestions for incorporating speckle decorrelation data to characterize a particular experiment.

4.8 Summary

Starting intensity on the detector and the sample stability are the main factors determining the level of enhancement that can be achieved through this optimization process. This implies that the reflectance properties of a particular sample determine the potential for enhancement in the specular direction and for beam steering ap-

plications. Sample stability given the current laboratory conditions can be assessed using the correlation coefficient when comparing images of the speckle pattern for a given SLM phase screen. Geometric considerations such as speckle size become a factor when lenses with longer focal lengths are used to focus the shaped beam onto the sample. For real-world application of this technique within indirect photography, the ultimate desire is to further distance the optical system from the reflecting surface and achieve enhancement in a variety of environmental conditions.

V. Discussion

5.1 Introduction

The research efforts detailed in this document are aimed at providing a proof of concept for the focusing of light scattered from diffuse reflectors using an SLM to assign phase delay to the impinging beam. All experiments are performed in setups which are practical within the context of indirect photography. The four main objectives which were introduced in Chapter 1 include this demonstration of a proof of concept, the nonmechanical steering of the focused spot, the identification of certain reflective properties which affect the results, and an outline detailing the progression required to advance this technique for implementation in indirect photography. This chapter serves to summarize the findings and resulting lessons learned and sketch out steps to be taken toward incorporating this technique into indirect photography.

5.2 Results Summary

Using the algorithm developed in Section 3.6 and the enhancement definition established in Section 2.4, the enhancement achieved on transmission for the white paint sample was 56.4. The more specular samples achieved enhancements between 67.7 and 122.3 in the specular direction. The more diffuse samples achieved lower enhancements in the specular direction, but higher enhancements in the direction of the surface normal relative to their corresponding specular direction enhancements for a beam incident at 45° .

5.3 Conclusions Drawn from Results

The demonstration of an SLM introducing phase delay patterns which inversely diffuse a HeNe beam to correct for diffuse scattering off of a reflective surface was

accomplished. High specular reflectance and sample stability contribute most significantly to achieving enhancement in the specular region, while diffuse scattering angle reflectance is significant in achieving comparable diffuse region enhancement. There is still a great deal of work to be done to implement this technique for reducing the problem of indirect photography to an application of dual photography, as outlined in Section 5.4.

5.4 Recommendations for Future Work

The recommendations for future work fall into three broad categories: (1) ways to improve the current setup to achieve higher enhancement values, (2) additional work required to more fully characterize the physics underlying the technique, and (3) the steps required to incorporate reflective inverse diffusion into indirect photography.

5.4.1 Algorithm Improvement.

Any change to the algorithm which searches the solution space and pinpoints a phase solution more quickly will incite greater enhancement in the focused spot. The time it takes to achieve a solution will always be at odds with the persistence time of the reflected speckle pattern. Calling the camera to take a single image and reading target intensity values into MATLAB from any of the SBIG camera's default photo formats take an exorbitant amount of time. The camera does not remain open while new SLM phase screens are generated, thus none of the operations are synchronized for efficiency. Given the same lab equipment, potential methods for better integrating the controlling software include but are not limited to: (1) building an interface using a MATLAB adaptor kit which is supplied with the MATLAB Image Acquisition Toolbox. At a minimum, this requires a substantial knowledge of the C++ programming languages. (2) Create a MEX interface with information

provided at the Mathworks, Inc. website. (3) Work with the software development consultants at AFIT to write the interface.

Establishing a routine which minimizes the time to focus to a sufficiently intense spot for scanning the hidden object is desirable. Other options for decreasing run time include implementing adaptive algorithm techniques for approaching an improved solution. As an example, for segments which do not contribute much to improving the target intensity, the algorithm could break up regions of the phase map into smaller segments. Figure 32 shows a 16x16 phase screen with a region broken into segments corresponding to a 32x32 phase screen.



Figure 32. Adaptive algorithm. Given certain indicators in the target intensity for a set of grouped pixels, break the pixel into subsets of smaller grouped pixels to efficiently increase enhancement.

5.4.2 Technique Improvement.

The calibration technique used to characterize the phase modulation of the SLM assumed a flat phase response across the SLM. In an effort to glean a set of pixel values which would best cover the range of phase delay, sets of fringe patterns corresponding to opposing gray scales were compared. To ensure that each and every pixel most closely covers the range of phase delay in even increments, one can further calibrate the SLM static aberration. Most often and notably caused by a backplane which is curved from manufacturing processes, static aberration can be tested for using interferogram analysis, a commercial interferometer, or parameterized phase retrieval

[17, 18, 13]. Interferogram analysis can be done with a Twyman-Green interferometer setup similar to the one used for fringe-shift analysis. This analysis would result in a LUT that is different for each pixel. To reduce the size of the LUT associated with the SLM for pixel-by-pixel conversion factors, the impinging beam size could be reduced to cover flatter regions of the SLM.

The performance of the enhancement process is highly dependent on the starting speckle intensity. The current setup is designed to resemble the setup used for inverse diffusion on transmission for easy comparison; however, half of the beam is dumped on the first pass through the NPBS onto the SLM, and more is lost upon its second reflection off the NPBS. Implementing an off-axis setup will ensure that the more power is delivered to the surface reflector for a given laser. Power considerations will become even more significant as the optical system is pushed back farther from the reflecting surface.

The decorrelation data presented in Section 4.7 was taken to characterize how the speckle pattern for a particular phase map decorrelates for a given sample and set of environmental conditions. The operations of an enhancement experiment are mimicked, suggesting that if an enhancement experiment had been performed instead, it would have suffered from the amount of decorrelation recorded. In order to disentangle the effect of the speckle decorrelation due to sample and environmental stability from the effect of changing other factors of interest, one could incorporate the decorrelation measurement technique directly into the enhancement technique. Defining a particular random phase map as a reference and periodically loading it onto the SLM throughout the enhancement process would provide the information necessary to establish a decorrelation metric for each test.

5.4.3 Reflective Inverse Diffusion Characterization.

Additional work must be done to pin down the contribution of various factors affecting the optimization process. All reflective inverse diffusion experiments were performed using a lens with a 1-meter focal length to focus the phase modulated beam onto the reflective sample. To glean a relationship between the spot size on the sample and the resulting enhancement, lenses with differing focal lengths should be used and their results compared.

Another important relationship may be the effect of varying starting intensity on the detector for a given sample within a given geometry. In general, samples with higher initial speckle pattern intensities achieved better results; however, exploring the relationship between starting intensity and resulting enhancement for a particular sample or among various samples may provide insight into enhancement limits imposed by certain material properties. Furthermore, a connection has been made between the BRDF and the resulting enhancement achieved for the samples involved. A precise relationship between a sample's BRDF and enhancement can be made by comparing enhancement for a range of angles to the scatter data provided by a Complete Angle Scatter Instrument (CASI).

5.4.4 Implementation in Indirect Photography.

As mentioned in the introduction, there is a progression of advancements in this research that must be made before reflective inverse diffusion could be incorporated to aid in indirect photography. The aim of indirect photography is to image objects hidden from both the camera and the light source; therefore, the SLM and detector which provides feedback to the SLM should not have access to a direct line of sight to the object. After improving the algorithm to achieve a higher intensity focused spot on the camera, which currently takes the place of the object to be imaged, a second

detector must be introduced to monitor interference patterns as the SLM modulates the beam. Eventually, the detector should be placed in close proximity with the other components of the indirect photography system while giving feedback to the SLM to focus onto spots on the object. An intermediate step could involve dividing the camera into two regions and focusing to a spot on one side while providing feedback to the SLM from the other.

5.5 Final Comments

The research detailed in this thesis completes the first step in reducing the complexity of the imaging process of indirect photography to the process used in dual photography. It establishes a proof of concept for focusing the light scattered off of diffuse surfaces using phase modulation and steering that focus. There is a significant amount of work to be done to advance this technique for realistic use in indirect photography, including improving the current technique, establishing precise relationships between enhancement and experimental factors, and eventually collocating the detector providing feedback to the SLM with the rest of the imaging system.

Appendix A. Reflective Inverse Diffusion MATLAB Function

Appendix A provides the main function which controls the SLM and the camera. The subroutines are listed separately in Appendix B so that the root function serves as a clear outline of the operations performed for the experiment.

```
1 function ExperimentNMatrix (Folder,PixelFile,NMatrix,PixRadius)
2 % Written by Jessica Schafer, 2Lt, AFIT/ENP
3 % Updated: 15 October, 2011
4 % All functions starting with "BNS_" are taken from the MATLAB SDK provided
5 % by BNS with minor alterations for the current context. NMatrix is a
6 % vector of phase map dimensions. The most common input for this thesis is
7 % [2 4 8 16 32]. PixRadius is determined by sample speckle size. PixelFile
8 % is the set of pixel values which will give the desired phase delay.
9
10 %% Initialize SLM.
11 BNS_OpenSLM;
12 BNS_SetPower(1);
13 ImageFrame = 0;           % Set PCI card memory slot value
14
15 %% Read in files which will be used in routine.
16 LUTMap = BNS_ReadLUTFile('C:\BNSMatlabSDK\LUT.Files\linear.LUT');
17 PixValues = dlmread(PixelFile);
18
19 %% Initialize parameters.
20 WinningMatrix=zeros(510,765);
21 ImageMatrix = round(255*rand(512));
22 Int=zeros(1,length(PixValues));
23 Count = 0;
24 CompactImageMatrix = round(255*rand(NMatrix(1)));
```

```

25
26 %% Record initial captures for each N value
27 RecordAvgStartIntensities (NMatrix,LUTMap,Folder)
28
29 %% Vary phase pixel by pixel
30
31 for h = 1:length(NMatrix)
32     N = NMatrix(h);
33     n = num2str(N);
34     H = num2str(h);
35     for i=1:N
36         I=num2str(i, '%.2d');
37         for j=1:N
38             %% Only vary pixel if it meets condition determining if it
39             %% falls within a circle of radius 7.62 mm.
40             if ((i≤N/2&&j≤N/2)&&(sqrt((N/2-i)^2+(N/2-j)^2)<N/2)) || ...
41                 ((i>N/2&&j≤N/2)&&(sqrt((N/2-(i-1))^2+(N/2-j)^2)<N/2)) || ...
42                 ((i≤N/2&&j>N/2)&&(sqrt((N/2-i)^2+(N/2-(j-1))^2)<N/2)) || ...
43                 ((i>N/2&&j>N/2)&&(sqrt((N/2-(i-1))^2+(N/2-(j-1))^2)<N/2))
44
45             for k=1:length(PixValues);
46                 [CompactImageMatrix,ImageMatrix]=...
47                     ChangePhaseMap(ImageMatrix,CompactImageMatrix,i,...
48                         j,PixValues(k),N);
49                 BNS_LoadImageFrame(ImageFrame,ImageMatrix,LUTMap);
50                 BNS_SendImageFrameToSLM(ImageFrame);
51                 ImageFrame=mod(ImageFrame + 1, 26);
52                 CaptureImage;
53                 CaptureMatrix=ReadSaveImage('Capture.sbig');
54                 Int(k)=CalculateIntensityProfile(CaptureMatrix,...
55                     PixRadius(h));
56                 %% Save the pixel value and corresponding image which

```

```

57         %% gives the highest intensity according to the target
58         %% function
59         if Int(k)==max(Int)
60             WinningMatrix = CaptureMatrix;
61         end
62
63         J=num2str(j, '%.2d');
64         if k==length(PixValues)
65             Count = Count + 1;
66             CompactImageMatrix = ...
67             DeterminePixelValue(PixValues, Int, i, j, ...
68             CompactImageMatrix);
69             dlmwrite(strcat...
70                 ('C:\BNSMatlabSDK\Schafer SLM Control\', ...
71                 Folder, '\OptImage', I, J, n, H, '.txt'), ...
72                 WinningMatrix, 'delimiter', '\t');
73             imagesc(WinningMatrix); colormap('hot');
74             title(strcat('Step', I, J, n, H));
75             dlmwrite(strcat...
76                 ('C:\BNSMatlabSDK\Schafer SLM Control\', ...
77                 Folder, '\TargetIntensity', I, J, n, H, ...
78                 '.txt'), Int, 'delimiter', '\t');
79         end
80     end
81 end
82 end
83 end
84 %% Save the phase screen which optimizes the target intensity.
85 dlmwrite(strcat('C:\BNSMatlabSDK\Schafer SLM Control\', Folder, ...
86     '\PhaseScreen', n, H, '.txt'), CompactImageMatrix, 'delimiter', '\t');
87 %% Expand compact image matrix of the previous size N to the next size N.
88     if h~=length(NMatrix)

```



```

89         CompactImChange = zeros(NMatrix(h+1));
90         for col = 1:N
91             for row = 1:N
92                 CompactImChange((2*row-1):(2*row),(2*col-1):(2*col))...
93                     =CompactImageMatrix(row,col);
94             end
95         end
96         CompactImageMatrix = CompactImChange;
97     end
98 end
99
100 %% Display last image.
101 imagesc(CaptureMatrix); colormap('hot');
102 figure; imagesc(CompactImageMatrix); colormap('gray');
103 BNS_CloseSLM;
104 end

```

Appendix B. Reflective Inverse Diffusion MATLAB

Subfunctions

```
1 function CaptureMatrix = ReadSaveImage (SBIG)
2 % Written by 2Lt Schafer, adapted from code written by Lt Col Mark
3 % Hoelscher for indirect photography. Updated 1 October, 2011.
4
5 %% Read in image file saved by SBIG camera and return as a matrix.
6 fid=fopen(SBIG);
7 fseek(fid,2048,'bof');
8 Image=fread(fid,[765,510],'ushort');
9 CaptureMatrix=Image';
10 fclose(fid);
11
12 end

1 function CompactImageMatrix = DeterminePixelValue(PV,Int,i,j,CompactImageMatrix)
2 %% Return the compact image matrix with the current pixel set to that which
3 %% maximizes the target intensity.
4 [I, Index] = max(Int);
5 CompactImageMatrix(i,j)=PV(Index);
6 end

1 function ImageMatrix=ExpandMatrix(StartMap,N)
2 %% Compute number of pixels of the SLM grouped into one effective pixel.
3 El = 512/N;
4 %% Expand compact matrix into image matrix for SLM
5 for col = 1:N
```

```

6     for row = 1:N
7         ImageMatrix(row*El-(El-1):row*El,col*El-(El-1):col*El) = StartMap(row,col);
8     end
9 end

1 function Int = CalculateIntensityProfileBeamSteer(Position,...
2     CaptureMatrix,PixRadius)
3 %% Written by Jessica Schafer, 2Lt, AFIT/ENP. Updated: 1 Nov, 2011.
4 %% Adaptation of CalculateIntensityProfile.m. Adaptation is included in
5 %% Appendix B instead because it has the main formula with extra
6 %% conditions.
7 SpotIntensity=0;
8 %% Input distances between center spot and corner spots to get corner
9 %% target intensity regions.
10 if Position == 1
11     CircDistVertical = 235;
12     CircDistHorizontal = 362;
13 elseif Position == 2
14     CircDistVertical = -235;
15     CircDistHorizontal = 362;
16 elseif Position == 3
17     CircDistVertical = 235;
18     CircDistHorizontal = -362;
19 elseif Position == 4
20     CircDistVertical = -235;
21     CircDistHorizontal = -362;
22 end
23 for j = 1:765
24     for i = 1:510
25         if((i≤510/2+CircDistVertical&&j≤765/2+CircDistHorizontal)...
26             &&(sqrt((510/2+CircDistVertical-i)^2+(765/2+...

```

```

27         CircDistHorizontal-j)^2)<PixRadius) ) || ...
28         ((i>510/2+CircDistVertical&&j≤765/2+CircDistHorizontal) ...
29         &&(sqrt((510/2+CircDistVertical-(i-1))^2+...
30         (765/2+CircDistHorizontal-j)^2)<PixRadius) ) || ...
31         ((i≤510/2+CircDistVertical&&j>765/2+CircDistHorizontal) ...
32         &&(sqrt((510/2+CircDistVertical-i)^2+(765/2+...
33         CircDistHorizontal-(j-1))^2)<PixRadius) ) || ...
34         ((i>510/2+CircDistVertical&&j>765/2+CircDistHorizontal) &&...
35         (sqrt((510/2+CircDistVertical-(i-1))^2+(765/2+...
36         CircDistHorizontal-(j-1))^2)<PixRadius) )
37         SpotIntensity=SpotIntensity+.5*CaptureMatrix(i,j);
38     end
39
40     if ((i≤510/2+CircDistVertical&&j≤765/2+CircDistHorizontal) ...
41         &&(sqrt((510/2+CircDistVertical-i)^2+(765/2+...
42         CircDistHorizontal-j)^2)<(3*PixRadius/4) ) ) || ...
43         ((i>510/2+CircDistVertical&&j≤765/2+CircDistHorizontal) ...
44         &&(sqrt((510/2+CircDistVertical-(i-1))^2+(765/2+...
45         CircDistHorizontal-j)^2)<(3*PixRadius/4) ) ) || ...
46         ((i≤510/2+CircDistVertical&&j>765/2+CircDistHorizontal) ...
47         &&(sqrt((510/2+CircDistVertical-i)^2+(765/2+...
48         CircDistHorizontal-(j-1))^2)<(3*PixRadius/4) ) ) || ...
49         ((i>510/2+CircDistVertical&&j>765/2+CircDistHorizontal) &&...
50         (sqrt((510/2+CircDistVertical-(i-1))^2+...
51         (765/2+CircDistHorizontal-(j-1))^2)<(3*PixRadius/4) ) )
52         SpotIntensity=SpotIntensity+.7*CaptureMatrix(i,j);
53     end
54
55     if ((i≤510/2+CircDistVertical&&j≤765/2+CircDistHorizontal) ...
56         &&(sqrt((510/2+CircDistVertical-i)^2+(765/2+...
57         CircDistHorizontal-j)^2)<(2*PixRadius/4) ) ) || ...
58         ((i>510/2+CircDistVertical&&j≤765/2+CircDistHorizontal) ...

```

```

59         &&(sqrt((510/2+CircDistVertical-(i-1))^2+(765/2+...
60         CircDistHorizontal-j)^2)<(2*PixRadius/4)))||...
61         ((i≤510/2+CircDistVertical&&j>765/2+CircDistHorizontal)...
62         &&(sqrt((510/2+CircDistVertical-i)^2+(765/2+...
63         CircDistHorizontal-(j-1))^2)<(2*PixRadius/4)))||...
64         ((i>510/2+CircDistVertical&&j>765/2+CircDistHorizontal)&&...
65         (sqrt((510/2+CircDistVertical-(i-1))^2+(765/2+...
66         CircDistHorizontal-(j-1))^2)<(2*PixRadius/4)))
67         SpotIntensity=SpotIntensity+.9*CaptureMatrix(i,j);
68     end
69     if((i≤510/2+CircDistVertical&&j≤765/2+CircDistHorizontal)...
70         &&(sqrt((510/2+CircDistVertical-i)^2+(765/2+...
71         CircDistHorizontal-j)^2)<(PixRadius/4)))||...
72         ((i>510/2+CircDistVertical&&j≤765/2+CircDistHorizontal)...
73         &&(sqrt((510/2+CircDistVertical-(i-1))^2+(765/2+...
74         CircDistHorizontal-j)^2)<(PixRadius/4)))||...
75         ((i≤510/2+CircDistVertical&&j>765/2+CircDistHorizontal)...
76         &&(sqrt((510/2+CircDistVertical-i)^2+(765/2+...
77         CircDistHorizontal-(j-1))^2)<(PixRadius/4)))||...
78         ((i>510/2+CircDistVertical&&j>765/2+CircDistHorizontal)...
79         &&(sqrt((510/2+CircDistVertical-(i-1))^2+(765/2+...
80         CircDistHorizontal-(j-1))^2)<(PixRadius/4)))
81         SpotIntensity=SpotIntensity+CaptureMatrix(i,j);
82     end
83
84     end
85 end
86 Int=SpotIntensity;
87 end

```

```

1 function RecordAvgStartIntensities (NMat,LUTMap,Folder)

```

```

2  %% Written by Jessica Schafer, 2Lt, AFIT/ENP. Updated 1 Dec, 2011.
3  %% Determine starting average speckle intensity with random phase screens.
4  ImageFrame = 0;
5  for Iteration = 1:length(NMat)
6      N = NMat(Iteration);
7      n = num2str(N, '%.2d');
8      for Start = 1:25
9          S = num2str(Start);
10         StartMap = round(255*rand(N));
11         ImageMatrix=ExpandMatrix(StartMap,N);
12         BNS_LoadImageFrame(ImageFrame, ImageMatrix, LUTMap);
13         BNS_SendImageFrameToSLM(ImageFrame);
14         ImageFrame=mod(ImageFrame + 1, 26);
15         CaptureImage;
16         InitialCapture = ReadSaveImage('Capture.sbig');
17         dlmwrite(strcat('C:\BNSMatlabSDK\Schafer SLM Control\',Folder, '\Initial',n,S, '.t
18             InitialCapture, 'delimiter', '\t');
19         imagesc(InitialCapture);colormap('hot'); title(strcat('Initial',n,S));
20     end
21 end
22 end

```

Appendix C. Surface Profiles of Reflectors

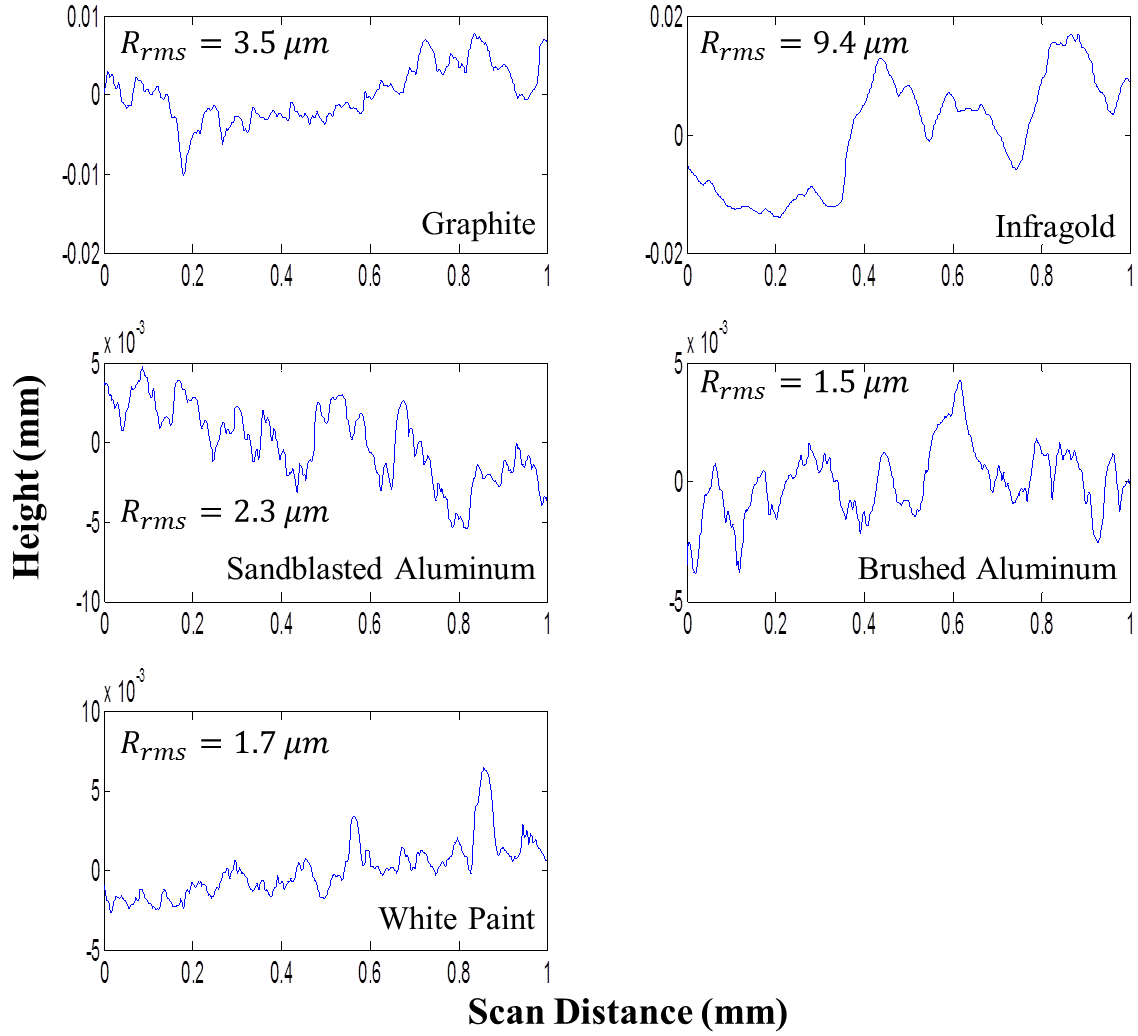


Figure 33. Surface profiles for each of the five samples measured with a Tencor Alpha Step 1000 profilometer. The RMS surface roughness R_{rms} is given for each sample.

Appendix D. Relative Intensity Plots and Images

The top half of each data subset displays the speckle pattern from a portion of the detector center for phase screens of $N = 4$, $N = 8$, $N = 16$, and $N = 32$. The pattern is normalized to the average starting intensities and plotted on a logarithmic scale. The bottom half shows the center row of intensities from the top half associated with each phase screen. Each of these corresponds to the final iteration—not necessarily the most optimal iteration—for its respective phase screen dimensions.

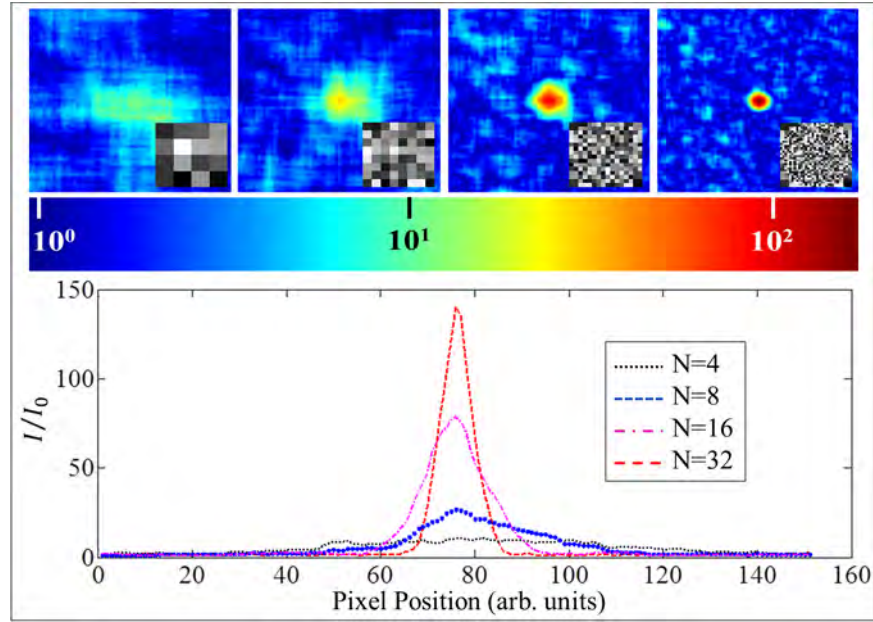


Figure 34. Relative intensity data for brushed aluminum.

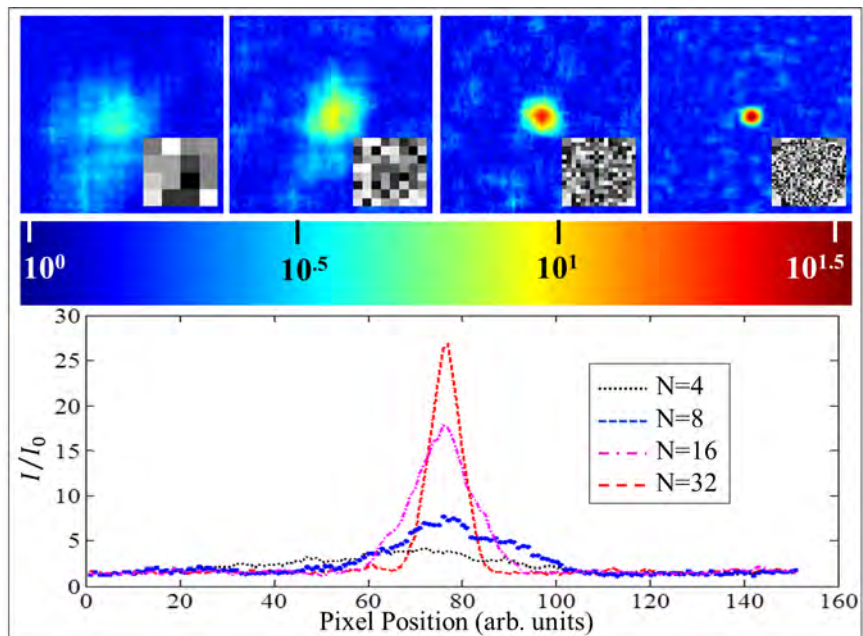


Figure 35. Relative intensity data for sandblasted aluminum.

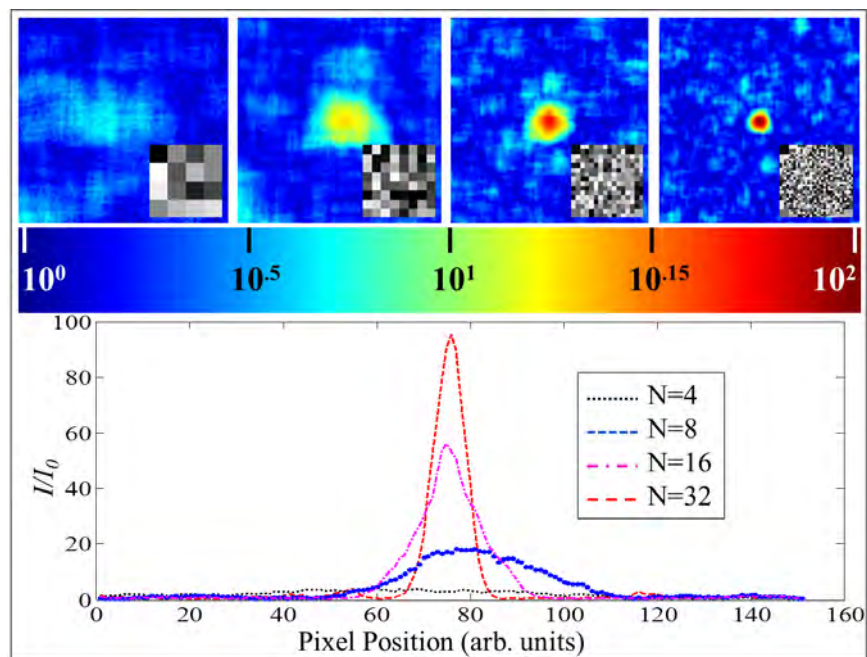


Figure 36. Relative intensity data for infragold.

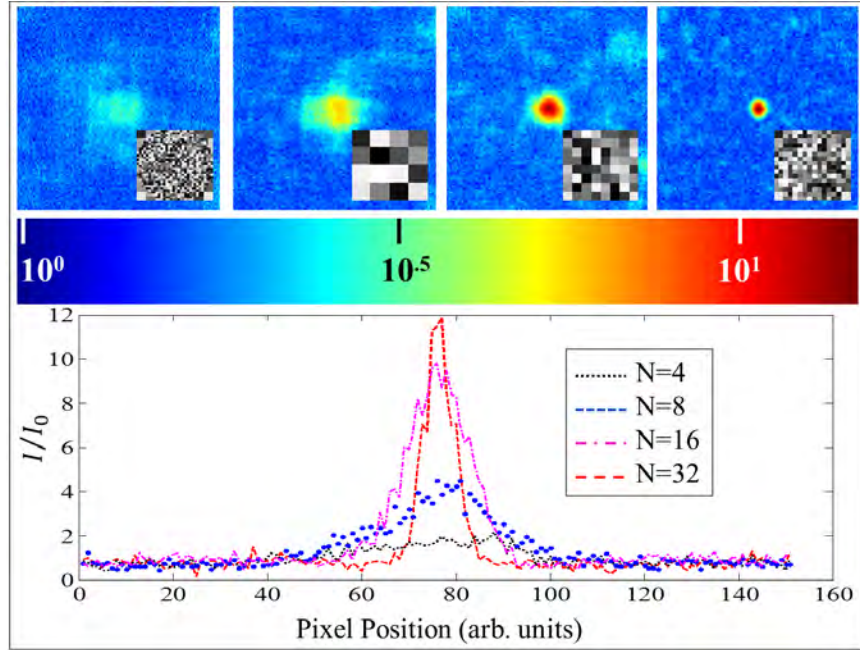


Figure 37. Relative intensity data for white paint on reflection.

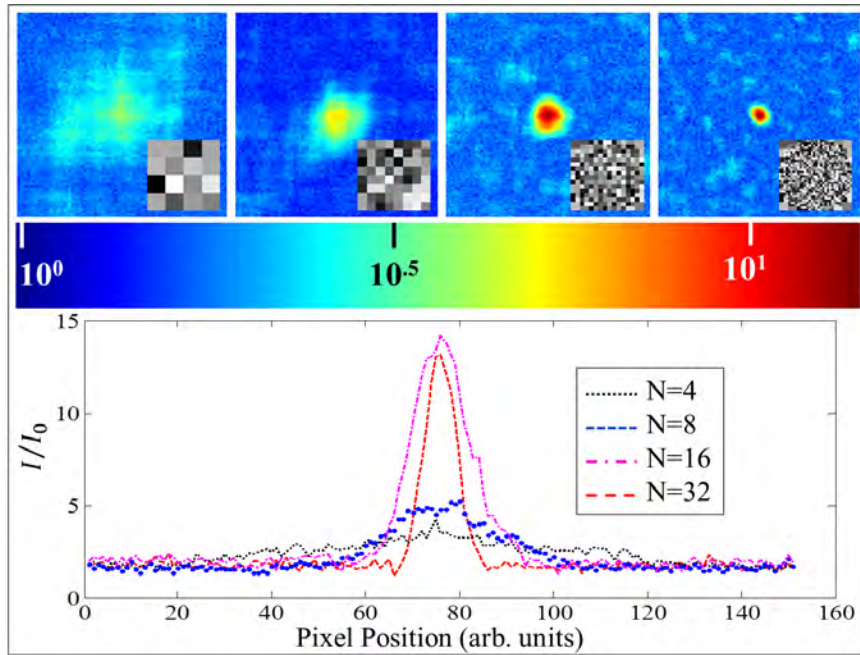


Figure 38. Relative intensity data for graphite.

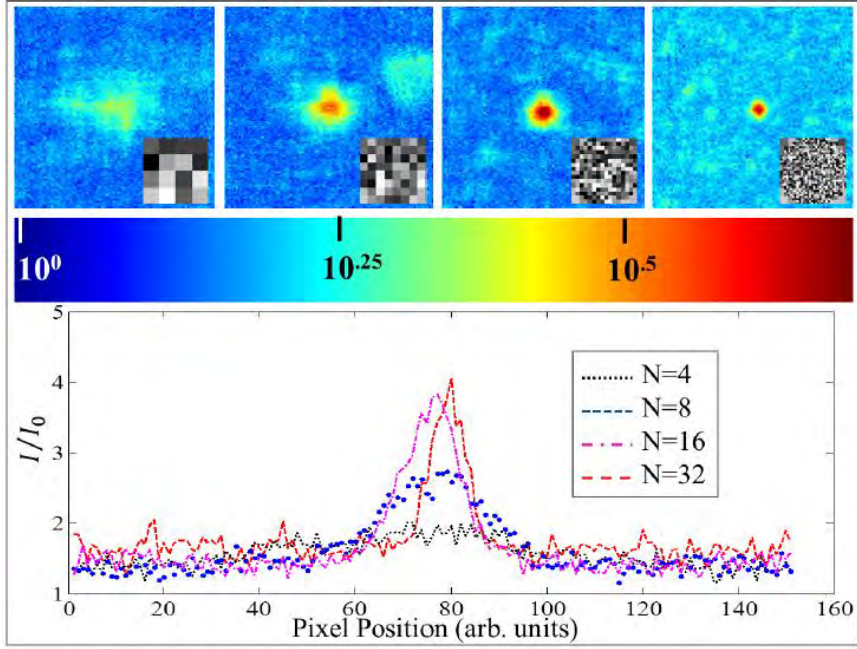


Figure 39. Relative intensity data for spectralon.

Bibliography

- [1] Hoelscher, M.G. and M.A. Marciniak. “Restoration of scene information reflected from a non-specular surface”. *Proceedings of SPIE*, volume 7792, 77920L. 2010.
- [2] Hoelscher, M.G. *Restoration of Scene Information Reflected from Non-Specular Media*. Technical report, DTIC Document, 2011.
- [3] Vellekoop, I.M. “Controlling the propagation of light in disordered scattering media”. *Arxiv preprint arXiv:0807.1087*, 2008.
- [4] Sen, P., B. Chen, G. Garg, S.R. Marschner, M. Horowitz, M. Levoy, and H. Lensch. “Dual photography”. *ACM SIGGRAPH 2005 Papers on SIGGRAPH 05*, 24(3):745–755, 2005.
- [5] Aulbach, J., B. Gjonaj, P.M. Johnson, A.P. Mosk, and A. Lagendijk. “Control of light transmission through opaque scattering media in space and time”. *Physical Review Letters*, 106(10):103901, 2011.
- [6] Vellekoop, IM and AP Mosk. “Phase control algorithms for focusing light through turbid media”. *Optics Communications*, 281(11):3071–3080, 2008.
- [7] Wick, D.V., B.E. Bagwell, W.C. Sweatt, W.D. Cowan, O.B. Spahn, G.L. Peterson, T. Martinez, S.R. Restaino, J.R. Andrews, C.C. Wilcox, et al. “Lightweight, active optics for space and near space”. *The Advanced Maui Optical and Space Surveillance Technologies Conference*, volume 1, 13. 2006.
- [8] Bagwell, B.E., D.V. Wick, R. Batchko, J.D. Mansell, T. Martinez, S.R. Restaino, D.M. Payne, J. Harriman, S. Serati, G. Sharp, et al. “Liquid crystal based active optics”. *Proc. SPIE*, volume 6289, 628908–12. 2006.
- [9] Resler, DP, DS Hobbs, RC Sharp, LJ Friedman, and TA Dorschner. “High-efficiency liquid-crystal optical phased-array beam steering”. *Optics letters*, 21(9):689–691, 1996.
- [10] Palmer, J.M., B.G. Grant, and Society of Photo-optical Instrumentation Engineers. “The art of radiometry”. SPIE, 2010.
- [11] Courreges-Lacoste, G.B., J.G. Schaarsberg, R. Sprik, and S. Delwart. “Modeling of Spectralon diffusers for radiometric calibration in remote sensing”. *Optical engineering*, 42:3600, 2003.
- [12] Yang, Z.P., L. Ci, A. James, S.Y. Lin, and P.M. Ajayan. “Experimental observation of an extremely dark material made by a low-density nanotube array”. *Nano letters*, 8(2):446–451, 2008.

- [13] Zhang, H., J. Zhang, and L. Wu. “Evaluation of phase-only liquid crystal spatial light modulator for phase modulation performance using a Twyman–Green interferometer”. *Measurement Science and Technology*, 18:1724, 2007.
- [14] Vellekoop, IM and AP Mosk. “Focusing of light by random scattering”. *Arxiv preprint cond-mat/0604253*, 2006.
- [15] Dereniak, E.L. and G.D. Boreman. *Infrared detectors and systems*, volume 306. Wiley New York, 1996.
- [16] Cheok, G.S., K.S. Saidi, and M. Franaszek. “Target penetration of laser-based 3D imaging systems”. *Society of Photo-Optical Instrumentation Engineers (SPIE) Conference Series*, volume 7239, 8. 2009.
- [17] Schmidt, J.D., M.E. Goda, and B.D. Duncan. “Aberration production using a high-resolution liquid-crystal spatial light modulator”. *Applied optics*, 46(13):2423–2433, 2007.
- [18] Xun, X. and R.W. Cohn. “Phase calibration of spatially nonuniform spatial light modulators”. *Applied optics*, 43(35):6400–6406, 2004.

REPORT DOCUMENTATION PAGE

Form Approved
OMB No. 0704-0188

The public reporting burden for this collection of information is estimated to average 1 hour per response, including the time for reviewing instructions, searching existing data sources, gathering and maintaining the data needed, and completing and reviewing the collection of information. Send comments regarding this burden estimate or any other aspect of this collection of information, including suggestions for reducing this burden to Department of Defense, Washington Headquarters Services, Directorate for Information Operations and Reports (0704-0188), 1215 Jefferson Davis Highway, Suite 1204, Arlington, VA 22202-4302. Respondents should be aware that notwithstanding any other provision of law, no person shall be subject to any penalty for failing to comply with a collection of information if it does not display a currently valid OMB control number. **PLEASE DO NOT RETURN YOUR FORM TO THE ABOVE ADDRESS.**

1. REPORT DATE (DD-MM-YYYY) 22-03-2012			2. REPORT TYPE Master's Thesis		3. DATES COVERED (From — To) May 2011 — Mar 2012	
4. TITLE AND SUBTITLE THE FOCUSING OF LIGHT SCATTERED FROM DIFFUSE REFLECTORS USING PHASE MODULATION					5a. CONTRACT NUMBER	
					5b. GRANT NUMBER	
					5c. PROGRAM ELEMENT NUMBER	
6. AUTHOR(S) Schafer, Jessica, 2Lt, USAF					5d. PROJECT NUMBER	
					5e. TASK NUMBER	
					5f. WORK UNIT NUMBER	
7. PERFORMING ORGANIZATION NAME(S) AND ADDRESS(ES) Air Force Institute of Technology Graduate School of Engineering and Management (AFIT/EN) 2950 Hobson Way WPAFB OH 45433-7765					8. PERFORMING ORGANIZATION REPORT NUMBER AFIT/APPLPHY/ENP/12-M10	
9. SPONSORING / MONITORING AGENCY NAME(S) AND ADDRESS(ES) Air Force Office of Scientific Research/RSE Attn: Dr. Kent Miller 875 N. Randolph St. Arlington, VA 22203 Comm:(703) 696-8426					10. SPONSOR/MONITOR'S ACRONYM(S) AFOSR	
					11. SPONSOR/MONITOR'S REPORT NUMBER(S)	
12. DISTRIBUTION / AVAILABILITY STATEMENT DISTRIBUTION STATEMENT A. APPROVED FOR PUBLIC RELEASE; DISTRIBUTION UNLIMITED.						
13. SUPPLEMENTARY NOTES						
14. ABSTRACT “Indirect photography” was recently demonstrated for imaging hidden scene information through the collection and radiometric modeling of light reflecting off of visible reflecting surfaces. The ability to focus the beam that reflects off the visible surface to a tight spot on the hidden object is theorized to simulate a direct line of sight from the light source to the object, reducing the radiometric model to that of the previously demonstrated dual photography. Experiments involving the focusing of light transmitted through highly scattering media have been adapted to the case of reflection. The focusing of a HeNe laser reflected off diffusely scattering surfaces to a tight spot is demonstrated using phase control. A liquid crystal spatial light modulator assigns pixelated phase delay to the beam to conjugate the scattering properties of the reflector. Intensity enhancement values between 13.8 and 122.3 are achieved for the surfaces studied. Samples with relatively strong specular reflection achieve higher enhancement for a given geometry. More diffusely reflecting materials achieve higher enhancement in regions of nonspecular scatter, facilitating non-mechanical beam steering.						
15. SUBJECT TERMS Phase Modulation, Indirect Photography, Inverse Diffusion, BRDF, Scattering, Liquid Crystal Spatial Light Modulator, Beam Steering, Enhancement						
16. SECURITY CLASSIFICATION OF:			17. LIMITATION OF ABSTRACT	18. NUMBER OF PAGES	19a. NAME OF RESPONSIBLE PERSON	
a. REPORT	b. ABSTRACT	c. THIS PAGE			Dr. Michael Marciniak	
U	U	U	U	78	19b. TELEPHONE NUMBER (include area code) (937) 255-3636; michael.marciniak@afit.edu	